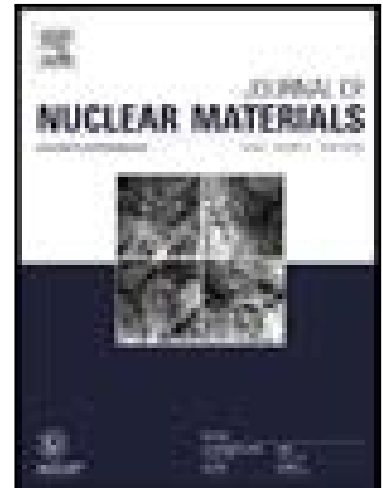


Journal Pre-proof

Understanding Radiation Effects in Friction Stir Welded MA956 using Ion Irradiation and a Rate Theory Model

E. Getto , N. Nathan , J. McMahan , S. Taller , B. Baker

PII: S0022-3115(22)00026-5
DOI: <https://doi.org/10.1016/j.jnucmat.2022.153530>
Reference: NUMA 153530



To appear in: *Journal of Nuclear Materials*

Received date: 1 October 2021
Revised date: 5 January 2022
Accepted date: 9 January 2022

Please cite this article as: E. Getto , N. Nathan , J. McMahan , S. Taller , B. Baker , Understanding Radiation Effects in Friction Stir Welded MA956 using Ion Irradiation and a Rate Theory Model, *Journal of Nuclear Materials* (2022), doi: <https://doi.org/10.1016/j.jnucmat.2022.153530>

This is a PDF file of an article that has undergone enhancements after acceptance, such as the addition of a cover page and metadata, and formatting for readability, but it is not yet the definitive version of record. This version will undergo additional copyediting, typesetting and review before it is published in its final form, but we are providing this version to give early visibility of the article. Please note that, during the production process, errors may be discovered which could affect the content, and all legal disclaimers that apply to the journal pertain.

© 2022 Published by Elsevier B.V.

15 Highlights

- 16 • Coarsening of welded dispersoids noted at higher irradiation temperatures.
- 17 • Any amount of welding increased void swelling, with maximum swelling of 0.5%.
- 18 • The dislocation behavior was inconsistent between base material and welded sample.

19

20

21 Abstract:

22 An outstanding challenge in the manufacturing and joining of oxide dispersion strengthened
23 steels is retaining the nanofeatures in the alloy throughout the fabrication and welding process. MA956
24 was friction stir welded with two different sets of welding parameters, resulting in a medium and high
25 heat input. After welding, 5 MeV Fe⁺⁺ ion irradiations were performed at doses ranging from 50 to 200
26 dpa in the temperature range of 400 to 500 °C. Post-irradiation characterization was performed with
27 scanning transmission electron microscopy and energy-dispersive x-ray spectroscopy to investigate the Y-
28 Al-O dispersoids, voids, and dislocations. After welding, the dispersoid microstructure coarsened,
29 resulting in fewer and larger dispersoids regardless of heat input. After irradiation, the dispersoid behavior
30 in the welded material was sensitive to temperature, exhibiting growth behavior attributed to Ostwald
31 coarsening at 500 °C but a mixture of nucleation and more muted growth at 400 and 450 °C, attributed to
32 competing mechanisms of radiation-enhanced diffusion and Ostwald coarsening. Void swelling correlated
33 to heat input; being more prevalent in the welded conditions occurring at lower doses and in higher values
34 relative to the base material. The low values of swelling despite microstructure coarsening caused by
35 welding demonstrate the excellent swelling resistance of MA956, even after welding with the highest
36 swelling values of 0.5% noted in the stir zone high heat input condition at 450 °C, 200 dpa. The
37 dislocation behavior was inconsistent: the strongest trend was that network density is higher for welded
38 versus base material, and an increase in loop diameter with temperature was observed. A rate theory
39 model based on the observed microstructure suggests at high temperature interstitial loss to sinks was
40 more likely to be dominant compared to mutual annihilation via point defect recombination, because of an
41 increase of the radiation diffusion coefficient with temperature regardless of initial welded microstructure.

42 1. Introduction

43 While stainless steels have been used successfully as structural materials in the past in light-water
44 and fast reactors [1,2], a variety of other materials such as ferritic-martensitic alloys, dual-phase alloys,
45 and oxide dispersion strengthened (ODS) ferritic alloys have been proposed and studied for future reactor
46 design concepts. One outstanding challenge is the manufacturing and joining of these advanced
47 materials—in particular, retaining the nanofeatures in the alloy throughout the fabrication and welding
48 process. Specifically, traditional fusion welding melts the material and disrupts the oxide particle
49 morphology [3], rendering it unsuitable as a joining technique. Furthermore, welding is deleterious for
50 nanofeatured alloys (NFAs) because welding can cause grain growth at the weld and the nearby heat-
51 affected zone and thus weaken the weld. Friction stir welding was initially developed for aluminum alloys
52 that also make use of precipitate strengthening [4]. It has further been applied successfully to other alloys,
53 including a variety of ODS steels, and has been studied extensively [5–9] as a joining technique.
54 However, the combined effect of welding and irradiation is of great interest to the reactor community, and
55 the number of studies and experimental conditions is sparse.

56 Ion irradiation has been shown to not only successfully emulate the irradiated reactor
57 microstructure, but also in creating systematic single parameter experiment matrices [10,11]. The benefit
58 of single parameter experiments is that they can unfold mechanistic behavior of individual microstructure
59 features and the co-evolution of the microstructure as a whole [12]. However, there are very few studies
60 [13–16] that address the combined effects of friction stir welding and irradiation, especially at
61 temperatures and doses suitable to emulate structural materials in a nuclear reactor environment.
62 Additionally, there is no study of the irradiation of multiple heat input welding conditions. Using multiple
63 welding conditions represents an opportunity to study the effect of the starting microstructure with the
64 same elemental composition on microstructure evolution. Therefore, the objective of the research
65 documented in this paper is to determine the effect of the combination of welding and ion irradiation on
66 the microstructure co-evolution of an ODS MA956 steel. This objective is accomplished by a systematic
67 dataset of ion irradiations at reactor relevant conditions (400–500 °C: 50–200 dpa) and microstructure
68 characterization to understand the changes in co-evolution between welded and base material, and finally,
69 application of a rate theory model to explain the resulting irradiation behavior.

70 2. Experiment

71 MA956 was provided by Lawrence Livermore National Laboratory in the form of a fine-grained
72 unrecrystallized steel plate [3]. The composition is given in Table 1. MA956 was canned and extruded at
73 1100 °C and hot rolled in three passes at 1100 °C over the course of 4 hours with reheating to 1100 °C 30
74 minutes before and after each rolling pass, resulting in a 4 mm thick plate. The ODS alloy of interest in
75 this study, MA956, was friction stir welded [17–19] and was irradiated in a previous study using 5 MeV
76 Fe^{++} ions for a single welding condition at 450 °C at 1 and 25 dpa [13] with a more extensive temperature
77 and high dose experimental matrix for the base material only [20].

78 2.1. Friction Stir Welding

79 MegaStir Technologies, now Mazak MegaStir, performed the friction stir welding process [3, 19].
80 The plunge force was maintained at 17.8 kN. The tool was fabricated from an MS 80 grade of
81 polycrystalline boron nitride (PCBN) using a convex scroll shoulder step spiral that did not require tilt.
82 Because of the difficulty of this weld process, a single bead-on-plate was run on plates of MA956 rather
83 than attempting to join two different base materials. Two heat input levels were selected and were
84 achieved by differing the tool rotation rate and tool traverse speed. For the medium heat input, the tool

85 was rotated at 300 rotations per minute (RPM), and the tool traverse rate was 50 mm per minute
86 (MMPM), and for the high heat input the tool rotation and traverse rate were 500 RPM and 25 MMPM,
87 respectively. Both conditions resulted in fully consolidated welds. Full details on the microstructure and
88 mechanical properties can be found in the literature [17,18]. For simplicity, the base material will be
89 referred to as *BM*, the medium heat input condition will be referred to as *SZ-M*, and the high heat input
90 condition will be referred to as *SZ-H*. The grain structure was previously analyzed in [18]. The *BM*, *SZ-*
91 *M*, and *SZ-H* had average grain diameters of 0.89 μm , 4.16 μm and 12.5 μm , respectively; all grains
92 remained ferritic in nature. Grain size was determined using electron backscatter diffraction (EBSD),
93 based on the paper by Baker et al. [3]. The as-received diameter and number density of the dispersoids for
94 *SZ-M* and *SZ-H* were 18.4 nm and $5.21 \times 10^{20} \text{ m}^{-3}$ and 19.7 nm and $2.01 \times 10^{20} \text{ m}^{-3}$, respectively, using
95 scanning transmission electron microscopy (STEM) [13].

96 2.2. Ion Irradiation

97 The irradiation and characterization procedures were identical to those used in the paper by Getto
98 et al. [20], which presented the base material results only, but they are included here as a baseline for
99 comparison. Prior to irradiation, 20 mm \times 2 mm \times 1.5 mm samples were excised from the plate using
100 electrical discharge machining. Polishing was performed using SiC paper up to 2400 grit followed by
101 diamond polishing down to 0.3 μm diamond solution. A final polishing step on a vibratory polisher using
102 0.02 μm silica solution for at least 2 hours was performed. Irradiations were performed at the Michigan
103 Ion Beam Laboratory, with either a 1.7 MV Tandem (Maize) or a 3 MV Pelletron (Wolverine) accelerator
104 utilizing 5 MeV Fe^{++} ions with a raster scanned beam. The raster scanning was performed with a raster
105 frequency of 2016 Hz along the vertical direction and 255 Hz horizontally for full coverage of the
106 irradiated area every 3.92 ms. Dose was calculated at a depth of 600 nm using the Quick Kinchin Pease
107 Mode in SRIM with displacement damage of 40 eV [21]. Dose rates varied between 0.7 and 1.1×10^{-3}
108 dpa/s. Samples were irradiated to 50 and 100 dpa at 400 and 500 $^{\circ}\text{C}$ and to 50, 100, and 200 dpa at 450
109 $^{\circ}\text{C}$. The *SZ-M* sample was not included in the 450 $^{\circ}\text{C}$: 50 dpa irradiation. Temperatures were maintained
110 and monitored using an infrared camera and a LabVIEW-controlled cartridge heater, and the temperature
111 was kept within $2\sigma < 5^{\circ}\text{C}$ over the course of the irradiation. Pressures in the target chamber were
112 maintained between 10^{-7} and 10^{-8} torr.

113 2.3. Microstructure Characterization

114 Transmission electron microscopy (TEM) lamellae were prepared using the Focused Ion Beam
115 (FIB) liftout method [22] and were thinned to electron transparency and cleaned with a final 5 kV polish.
116 The samples were taken from the middle of the stir zone, oriented in the middle of the stir zone
117 horizontally and in the middle of the stir zone depth. Lamellae were taken in cross section with Pt
118 deposited on the surface to protect the surface to enable depth profiling. An effort was made to have at
119 least two liftouts per irradiation condition. STEM bright field (BF) and high-angle annular dark field
120 (HAADF) images were taken using either a JEOL 2100F TEM/STEM or an FEI Tecnai TF30-FEG
121 Super-Twin STEM analytic electron microscope with a view field of approximately $1.2 \mu\text{m} \times 1.2 \mu\text{m}$.
122 Tilting of the sample was used to limit diffraction contrast such that all dispersoids were visible.
123 Thickness was measured using the electron energy loss spectroscopy (EELS) zero loss method [23].
124 HAADF images were used for counting of dispersoids. After imaging, dispersoids were characterized in
125 100 nm depth “bins” from the surface to 1000 nm. The region of 500–700 nm was selected to bracket the
126 reported nominal dose at 600 nm. The procedure for error analysis was the same as described in detail by
127 Getto et al. for irradiation-induced voids caused by the similarity between voids and dispersoids in

128 imaging [24]. The resolution limit for dispersoids and voids counted in this study was taken as 2 nm,
129 which corresponded to approximately 4 pixels.

130 Voids and dispersoids appeared similar under HAADF imaging. HAADF imaging is based upon
131 Z contrast, whereas lower Z phases appear as black or dark gray relative to the higher Z matrix [25].
132 Since smaller voids or dispersoids have relatively similar Z values compared to the Fe-Cr matrix, it is not
133 immediately clear from just the HAADF image whether a dark feature is a void or dispersoid. Fresnel
134 contrast imaging (also known as phase contrast imaging [26] and the over/under focus technique) was not
135 used because it could not by itself distinguish between voids and dispersoids at small sizes. Thus, to
136 discriminate between dispersoids and voids, energy-dispersive x-ray spectroscopy (EDS) scans with
137 correlated HAADF and BF images were taken using a SuperX EDS system on an FEI Titan ChemiSTEM
138 FEG-STEM. This was performed at the Irradiated Materials Characterization Laboratory (IMCL) at Idaho
139 National Laboratory so that the HAADF images could be compared to the elemental distribution. A “dark
140 feature” was determined to be a void if the dark area in the HAADF image corresponded with an area
141 depleted in Fe, O, and Ti. This means that the feature was not a dispersoid or preexisting carbide. Voids
142 did not form in many experimental conditions and did not affect the dispersoid data collection and
143 distributions. For the case in which voids were identified, at least 3 EDS area scans of $\sim 1200 \text{ nm} \times 1200$
144 nm were scanned to ensure that no voids were misidentified as dispersoids in the HAADF-only images.
145 Because of the limitation in number of scans, the linear area examined decreased from $\sim 21 \mu\text{m}$ to $3.2 \mu\text{m}$.
146 Thus, a larger depth range of 300 to 1,000 nm was used to improve dispersoid statistics. Dislocation loops
147 and network were imaged using STEM BF between approximately 500 and 700 nm from the irradiated
148 surface according to the procedure from [27]. On-zone or near-zone STEM imaging was chosen as on-
149 zone STEM imaging simultaneously excites all possible diffraction vectors for the zone axis, as well as
150 relaxes the g-b invisibility criterion allowing for faint contrast from in-plane $a[100](200)$ loops [28].
151 Thus, all possible dislocation morphologies, including line dislocations, can be imaged in a single
152 micrograph. Network line length was calculated using the procedure described in [29,30]. Error for the
153 loop diameter was taken as the resolution of the instrument similar to the analysis for void and dispersoids
154 noted above. The loop number and line density were taken as 20% to account for variation in thickness as
155 well as counting areas. The data repository for this work is located at [31].

156 2.4. Point Defect Model

157 To calculate the point defect concentrations, a standard rate equation for the change in defect
158 concentration of either interstitials and vacancies with time was used in the paper by Parish et al. [32]:

$$159 \quad \frac{dC_{(i,v)}}{dt} = K_0 - K_{iv}C_i(C_v + C_{v,T}) - k_{(i,v)}^2 D_{(i,v)}C_{(i,v)}, \quad (1)$$

160 where $k_{(i,v)}^2$ is the sink strength for either vacancies or interstitials and $D_{(i,v)}$ is the diffusion coefficient
161 for the point defect specie. The sink strengths for interstitials and vacancies were calculated for each
162 irradiation condition using the microstructure features characterized herein. For each specie, the total sink
163 strength is the sum of the sink strengths of the individual measured sinks:

$$164 \quad k_v^2 = k_{dis}^2 + k_{cav}^2 + k_{gb}^2 + k_{prec}^2, \quad (2)$$

$$165 \quad k_i^2 = k_{dis}^2(1 + Z) + k_{cav}^2 + k_{gb}^2 + k_{prec}^2, \quad (3)$$

166 where k_{cav}^2 is the sink strength from cavities and bubbles (voids in this case), k_{gb}^2 is the grain boundary
167 sink strength, k_{prec}^2 is the dispersoid sink strength, and the total dislocation sink strength, k_{dis}^2 , is
168 multiplied by an interstitial bias factor (Z). The calculation of sink strengths from the irradiated

169 microstructure is based on the formula presented by Was [32]. From the values of diameter and density in
 170 the dislocation loop size distributions, a total loop line length (equivalent sink strength) was calculated.
 171 The sink strength of the dislocation loops was calculated using the following equation:

$$172 \quad k_{dis}^2 = k_{network}^2 + k_{loop}^2 = \rho_{network} + \pi \sum_{i=0}^D d_i \rho_i, \quad (4)$$

173 where $\rho_{network}$ is the dislocation network density, ρ_i is the number density of dislocation loops of diameter
 174 d_i in the dislocation loop size distribution, and D is the maximum dislocation loop diameter observed. As
 175 discussed in [28, 29], a higher boundary misorientation angle leads to a higher sink strength, and thus the
 176 different types of boundaries in ferritic-martensitic steels will lead to differences in sink strength. As a
 177 conservative estimate, boundaries were treated as prior austenite grain boundaries (high sink strength)
 178 using the equation for the strongest sink strength boundaries with small grain diameters taken from Was
 179 [32] with a measured grain diameter of 4.16 μm and 12.5 μm for SZ-M and SZ-H, respectively [17]:

$$180 \quad k_{gb}^2 = \frac{24}{d^2}. \quad (5)$$

181 The grain boundary sink strength for BM was calculated in the paper by Getto et al. [20]. This sink
 182 strength was assumed to be constant throughout irradiation. The ODS dispersoids and voids both act as a
 183 neutral sink. Although several studies [35,36] suggest voids may have a bias for interstitials, the effective
 184 capture radius caused by the bias is expected to scale as $T^{-1/3}$ and fall off proportional to r^{-3} as is the case
 185 for voids. Thus, as the radius of a void or the irradiation temperature increase, the proportionality of the
 186 sink strength of a biased void to a neutral sink approaches unity. In this work, the voids are quite large
 187 and the temperature is fairly high leading to an estimation of about 5% bias for interstitials at maximum
 188 [35]. Thus, the sink strength can be calculated using

$$189 \quad k_{prec,cav}^2 = 2\pi \sum_{i=0}^D d_i N_i, \quad (6)$$

190
 191 where N_i is the density of dispersoids or cavities of diameter d_i , and D is the maximum diameter observed.
 192 The previously described equations were used with the time derivative in Equation (1) set to zero to solve
 193 for the steady-state concentration of interstitials and vacancies using a numerical solver in MATLAB.

194 Along with the point defect results, the effective diffusion coefficient for Y diffusion, which is
 195 expected to be the limiting process for because of its relatively slower diffusion than Al and O [37], was
 196 also calculated. The thermal diffusion for Y is

$$197 \quad D_{th,Y} = 0.1 \exp\left(-\frac{3.25eV}{k_B T}\right), \quad (7)$$

198 per the paper by Hin and Wirth [38]. The overall diffusion constant was calculated by

$$199 \quad D_Y^{irr} = \frac{C_V^{irr}}{C_{v,T}} D_{th,Y}, \quad (8)$$

200 where $C_{v,t}$ is calculated by

$$201 \quad C_{v,T} = \frac{1}{\Omega} \exp\left(\frac{S_f}{k}\right) \exp\left(\frac{-E_f^v}{kT}\right), \quad (9)$$

202 and C_V^{irr} is calculated by

$$C_V^{irr} = \frac{K_0}{k_{pt}^2 D_V}. \quad (10)$$

203
204 The parameters used for the rate theory calculations are included in Table 2. The uncertainty for
205 the calculations was done using standard error propagation techniques [39] from the uncertainty in the
206 input parameters. The parameterization utilized in Table 2 was determined by (1) identifying the range of
207 acceptable vacancy and formation energies [40–43] and (2) verifying that trends observed here were
208 insensitive to the range examined. This model was applied to the BM condition with results presented in
209 the paper by Getto et al. [20].

210 3. Results

211 3.1. Dispersoids

212 An example of the HAADF and BF images for the as-received and welded materials is provided
213 in Figure 2 as a baseline. With the addition of either the SZ-M or SZ-H welding parameters, there was
214 clear coarsening of the dispersoids (Figure 2a versus Figure 2b/c). The resulting grain boundary and
215 dispersoid sink strength of the as-received and irradiated microstructures are presented in Table 3, and the
216 dislocation network sink strength, which is the same as the measured line length, is shown in Table 4. The
217 sink strengths are compared with the baseline microstructure to elucidate the effect of welding only. First,
218 the high heat input (SZ-H) coarsened the dispersoids, increasing the diameter from 10.6 ± 1.0 nm to 19.7
219 ± 1.0 nm and decreasing the number density from $8.96 \pm 1.8 \times 10^{20} \text{ m}^{-3}$ to $2.01 \pm 0.4 \times 10^{20} \text{ m}^{-3}$, leading to
220 a commensurate decrease in overall sink strength. Although there was also dispersoid coarsening with the
221 SZ-M, the sink strength remained similar to that of the BM. Dislocation network sink strength was largest
222 in SZ-M ($1.84 \pm 0.6 \times 10^{14} \text{ m}^{-2}$) and similar in BM ($0.61 \pm 0.2 \times 10^{14} \text{ m}^{-2}$) and SZ-H ($0.53 \pm 0.2 \times 10^{14} \text{ m}^{-2}$).
223 The grain coarsening observed in the paper by Baker et al. [18] resulted in reduction of the grain
224 boundary sink strength from $3.03 \times 10^{13} \text{ m}^{-2}$ to $1.13 \times 10^{12} \text{ m}^{-2}$ and $1.54 \times 10^{11} \text{ m}^{-2}$. Only in the BM
225 sample was the grain boundary sink strength on the same order of magnitude as the dispersoids or
226 dislocation network.

227 The effect of irradiation is shown in the HAADF images for the BM (Figure 3)—which is
228 repeated as a benchmark from the paper by Getto et al. [20]—SZ-M in Figure 4 and for the SZ-H in
229 Figure 5, respectively. In Figure 4 and Figure 5, some dispersoids are marked with red arrows, and voids
230 are identified by white arrows. In general, dispersoid diameter tends to increase with increasing
231 irradiation temperature. For SZ-M at 100 dpa, there is a visible increase in dispersoid diameter from 400
232 °C (Figure 4c) to 500 °C (Figure 4e). Re-precipitation of the dispersoids is clearly observed after
233 irradiation compared to the as-welded materials (Figure 2b/c), which is consistent with lower dose results
234 at 450 °C, 1 and 25 dpa [13].

235 Voids and dispersoids appeared similar under HAADF imaging. For nearly all experimental
236 conditions, voids were not observed and thus did not affect the dispersoid data collection and
237 distributions. A selection of composition scans used in the void identification is shown in Figure 6 and
238 Figure 7 for SZ-M and SZ-H, respectively. For SZ-H, voids formed at all doses at 450 and 500 °C. For
239 SZ-M, voids occurred at 500 °C and 450 °C at 200 dpa only. For these cases, the dispersoid diameter and
240 number density were measured using the EDS scans instead of just the HAADF images (as described in
241 Section 2.3), ensuring that no voids were misidentified as dispersoids.

242 Dispersoids were quantified according to the procedure described in previous work [13, 20], and
243 the results are shown in Table 4. The initial dispersoid diameter distribution measured from the HAADF

244 images is presented in Figure 8 for BM (Figure 8a), SZ-M (Figure 8b), and SZ-H (Figure 8c). Two trends
 245 are notable. Regardless of irradiation temperature, both SZ-M and SZ-H have a flatter distribution relative
 246 to the results in the base material. The effect of temperature is most muted for BM (Figure 8a), which has
 247 a strong peak in the distribution, regardless of temperature. There appears to be more coarsening at 450
 248 °C and 500 °C for SZ-M (Figure 8b). Figure 8c shows SZ-H, which clearly shows more abundant and
 249 larger dispersoids with increasing temperature.

250 The mean dispersoid diameter as a function of dose at each temperature is plotted in Figure 9a for
 251 BM (solid blue), SZ-M (hatched red), and SZ-H (striped green). At 400 °C, the effect of dose on
 252 dispersoid diameter was muted. Although the diameter increased from 10.6 ± 1.0 nm up to 16.0 ± 1.0 nm
 253 for BM, SZ-M only grew from 18.4 ± 1.0 nm to 23.8 ± 1.0 nm and SZ-H from 19.7 ± 1.0 nm to 20.2 ± 1.0
 254 nm, indicating near stable behavior. At the higher temperatures, the effect of growth was much stronger,
 255 as shown for 450 °C and 500 °C, at which temperatures both SZ-M and SZ-H nearly doubled in average
 256 size from 0 to 100 dpa from 18.4 ± 1.0 nm and 19.7 ± 1.0 nm to 25.1 ± 1.0 nm and 32.2 ± 1.0 nm,
 257 respectively. The trends in growth were largely the same for both SZ-M and SZ-H, though in some cases
 258 (500 °C:50 dpa and 450 °C: 100 dpa) growth of dispersoids in the SZ-M surpassed that of SZ-H.

259 Figure 9a shows the number density versus dose at 400 °C. The BM consistently decreased with
 260 increasing dose across all temperatures. However, both SZ-M and SZ-H decreased with increasing dose at
 261 500 °C only. In contrast, at 400 °C, the SZ-M number density decreased from $5.21 \pm 0.5 \times 10^{20} \text{ m}^{-3}$ to
 262 $2.29 \pm 0.2 \times 10^{20} \text{ m}^{-3}$ from 0 to 50 dpa and then increased again to $5.43 \pm 0.5 \times 10^{20} \text{ m}^{-3}$. The number
 263 density with SZ-H initially increased from $2.01 \pm 0.2 \times 10^{20} \text{ m}^{-3}$ to $4.84 \pm 0.5 \times 10^{20} \text{ m}^{-3}$ then decreased to
 264 $3.52 \pm 0.4 \times 10^{20} \text{ m}^{-3}$ at 100 dpa. At 450 °C, the SZ-M tended to decrease with increasing dose, and
 265 number density for SZ-H tended to increase to 50 dpa ($4.34 \pm 0.4 \times 10^{20} \text{ m}^{-3}$) then decrease to 200 dpa
 266 ($2.36 \pm 0.2 \times 10^{20} \text{ m}^{-3}$).

267 3.2. Voids

268 Composition maps obtained with the SuperX EDS system are shown in Figure 10 with voids
 269 marked. The voids are the dark features, which represent depletion in all the major elements, and smaller
 270 voids are marked with red arrows. From these scans, voids and dispersoids were identified in the 300 to
 271 1,000 depth region and measured for void diameter, number density, swelling, dispersoid diameter, and
 272 number density, as presented in Section 3.1. The results are shown in Table 4 and Table 5. No voids
 273 formed at 400 °C. The BM did not form voids except at 450 °C, 200 dpa [20]. SZ-M formed voids at 450
 274 °C, 200 dpa (Figure 10a) and 500 °C, 50 and 100 dpa (Figure 10b/c). SZ-H formed voids at all doses at
 275 450 °C (Figure 10d–f) and 500 °C (Figure 10g/h). Voids nucleated primarily on the dispersoids or pre-
 276 existing titanium carbides. Despite the low number of voids formed, two trends are apparent. First, voids
 277 formed at more experimental conditions in SZ-H than SZ-M, and swelling values were the same or higher
 278 for all temperatures and dose—again demonstrating more void swelling resistance for SZ-M relative to
 279 SZ-H for these experimental parameters. Thus, the addition of any weld was deleterious to void swelling
 280 resistance.

281 3.3. Dislocations

282 A selection of images used for dislocation loop analysis is shown in Figure 11. Images are
 283 compared for all temperatures at 100 dpa only. Network line density was counted according to the
 284 concentric intercept method described by Xu [30]. The quantified data for dislocation loop diameter,
 285 number density, and network are shown in Figure 12. Regardless of welding condition, the loop diameter
 286 tended to increase with both dose and temperature (Figure 12a) as expected. For example, the loop

287 diameter increased from 23.8 ± 1.0 nm to 29.6 ± 1.0 nm to 52.7 ± 1.0 nm from 400, 450 and 500 °C,
 288 respectively, for SZ-M at 100 dpa. SZ-H, on the other hand, tended to be more inconsistent, with diameter
 289 decreasing with increasing dose at 400 and 500 °C from 50 to 100 dpa and at 450 °C from 48.3 ± 1.0 nm
 290 at 100 dpa to 23.4 ± 1.0 nm at 200 dpa.

292 Number density (Figure 12b) weakly correlated with temperature, with higher number density at
 293 400 °C relative to the larger temperatures for all welding conditions. At 400 °C, the loop number density
 294 increased with increasing dose for BM and SZ-M, remaining nearly within error bars for SZ-H. Similarly,
 295 the number density remained the same or decreased at 450 and 500 °C. SZ-M consistently had the highest
 296 loop number density. The network data are plotted in Figure 12c. With increasing dose, network tended to
 297 plateau at the highest doses, regardless of temperature. The main outlier was at 500 °C, 100 dpa, where
 298 there was a decrease in network line density for SZ-H from $2.5 \pm 0.6 \times 10^{14}$ m⁻³ at 50 dpa to $0.8 \pm 0.2 \times$
 299 10^{14} m⁻³ at 100 dpa.

300 4. Discussion

301 In this section, the evolution of each individual aspect of the microstructure is assessed, followed
 302 by how each feature interacts and co-evolves within the totality of the microstructure. Finally, the rate
 303 theory model is applied to the characterized microstructure, and results are presented to contextualize the
 304 effect of the as-received, welded, and evolving microstructures on defect behavior.

305 4.1. Dispersoids

306 There are several irradiation mechanisms affecting precipitates in general and dispersoids in
 307 particular, summarized in the paper by Wharry et al. [44]. First, ballistic dissolution can destabilize
 308 precipitates, ultimately leading to decreased diameter and number density. This mechanism is balanced by
 309 radiation enhanced diffusion, which can aid precipitate growth, coarsening, or re-precipitation; this has
 310 been observed in this alloy at 1 and 25 dpa [13]. To assess the strength of these two potential
 311 mechanisms, the dispersoid diameter and number density were examined and are presented in Figure 9.
 312 To reiterate, at all temperatures, BM demonstrated increased diameter and decreased number density with
 313 increasing dose that was consistent with Ostwald coarsening [20]. In contrast, dispersoid coarsening was
 314 observed only at 500 °C in SZ-M and SZ-H.

315 At 400 °C, the diameter remained mostly stable for both welding conditions, but the number
 316 density tended to decrease then increase for SZ-M, whereas it increased then decreased for SZ-H. At 450
 317 °C, the diameter for the SZ-M and SZ-H tended to increase and then plateau by 200 dpa, and the number
 318 density decreased with SZ-M, and for SZ-H, it increased then slightly decreased. This is consistent with
 319 nucleation of new dispersoids from either dispersoids that were dissolved during welding [13] or
 320 nucleation of smaller dispersoids from ballistic dissolution of larger dispersoids [40, 41]. From these
 321 trends, it is clear that coarsening becomes more dominant with increasing temperature, regardless of
 322 welding condition. Therefore, it is reasonable to identify Ostwald coarsening at the 500 °C and a mixed
 323 mechanism of radiation enhanced diffusion and ballistic dissolution at the lower temperatures for the
 324 welded sample. Mixed mechanisms like these have been observed in the literature [36, 39, 42, 43],
 325 especially ballistic dissolution combined with radiation-enhanced diffusion aiding recoil resolution of
 326 oxide dispersoids or nanoparticles.

327 Because there is a balance between the competing mechanisms, a further way to assess which
 328 mechanism is dominant in this alloy is by calculating a value for D_{irr}^Y , which ought to control migration

329 toward dispersoids. Y is expected to be limiting for dispersoid growth because it has a higher migration
 330 energy than Al, and O diffuses interstitially. D_{irr}^Y can be compared to a value for the ballistic dissolution
 331 coefficient [49] to determine which mechanism would be more dominant. The calculation method was
 332 adapted from Getto et al. and Lescoat et al. [20, 44] and is detailed in Section 2.4. At 100 dpa, D_{irr}^Y for
 333 SZ-M was 4.98×10^{-18} , 1.71×10^{-17} and $3.96 \times 10^{-17} \text{ cm}^2\text{s}^{-1}$ for 400, 450, and 500 °C, respectively. D_{irr}^Y
 334 for SZ-H were 3.42×10^{-18} , 1.55×10^{-17} and $5.31 \times 10^{-17} \text{ cm}^2\text{s}^{-1}$ for 400, 450, and 500 °C, respectively.
 335 These are compared to the BM values for D_{irr}^Y calculated by Getto et al. [20], which were 1.18×10^{-18} ,
 336 2.51×10^{-18} and $8.42 \times 10^{-18} \text{ cm}^2\text{s}^{-1}$ for 400, 450, and 500 °C, respectively. These values of D_{irr}^Y indicate
 337 that radiation-enhanced diffusion of Y is the strongest in BM, followed by SZ-M and SZ-H. The lower
 338 sink strength of the dispersoids after welding led to a relatively longer time for Y to diffuse to an existing
 339 dispersoid. Another observation is that radiation-enhanced diffusion of Y is lowest at the low
 340 temperatures, and thus, the propensity toward growth is the weakest. This is consistent with the results in
 341 noted above, in which the diameter of the dispersoids at 400 °C was approximately stable. The ballistic
 342 dissolution diffusion coefficient range was calculated by Getto et al. [20] and was in the range of $1.71 \times$
 343 $10^{-19} \text{ cm}^2\text{s}^{-1}$ to
 344 $5.12 \times 10^{-19} \text{ cm}^2\text{s}^{-1}$, for forward and backward recoils in the range of 400 to 500 °C. These values are
 345 independent of sink strength, unlike D_{irr}^Y , and would thus be independent of welding conditions, but note
 346 that the diffusion coefficients are much more similar for welded versus nonwelded and at lower
 347 temperature. Thus, the apparent stability at 400 °C for SZ-M and SZ-H and muted growth at 450 °C is
 348 likely a mixed mechanism of radiation-enhanced diffusion and ballistic dissolution.

349 4.2. Voids

350 Because of the low number of voids counted at several experimental conditions, the void data
 351 should be considered as general trends rather than precise swelling values. Even so, the void behavior was
 352 consistent with the literature. The voids nucleated primarily on the dispersoids or other secondary phases,
 353 which has been observed in MA956 [45, 46] and other alloys [52–54]. Previously, this was attributed to
 354 He trapped at the dispersoid/matrix interface [55,56], but since no He was used in these ion irradiation
 355 experiments, this shows that vacancies are trapped at dispersoids in a similar way even without He to
 356 promote nucleation. The diameter of voids tended to increase with temperature and dose, as expected [24,
 357 40, 50–53]. The actual values of swelling remained quite low, regardless of heat input. The BM
 358 demonstrated the lowest amount of swelling, with voids forming only at 450 °C, 200 dpa, whereas voids
 359 formed more readily for both SZ-M and SZ-H. Thus, void swelling resistance decreased with friction stir
 360 heat input. The largest amount of swelling (0.50%) occurred in the SZ-H sample at 450 °C, 200 dpa and
 361 remained low, especially when compared to austenitic alloys [60]. For SZ-M, the largest swelling value
 362 was observed at 500 °C, where void swelling was larger (0.01% and 0.11% for 50 and 100 dpa,
 363 respectively) than that at 450 °C, 200 dpa. This may indicate the peak swelling temperature is at 500 °C
 364 or higher for this ion irradiation condition. In contrast to the swelling resistance reported here, Guo et al.
 365 irradiated friction stir welded 12Cr ODS steel with 3 MeV Au ions [14] and observed voids in the BM but
 366 not the SZ at 500 °C, 2.7 dpa. It is critical to note that the BM grain diameter was larger than that of the
 367 SZ, whereas coarsening occurred with welding for both dispersoids and grains in this study. With friction
 368 stir welding of MA956 and similar alloys, the application of welding tends to coarsen a fine-grain
 369 structure [5, 55, 56], whereas an as-received coarse-grain structure tends to recrystallize [6, 9, 57]; these
 370 opposite responses depend on the initial microstructure. Since larger grains have a lower sink strength, the
 371 interiors of large grains are expected to have more voids, as well as a proportionally smaller void denuded
 372 zone near grain boundaries; again the smallest grained microstructure (BM) had the least amount of
 373 swelling reported here.

374 Other irradiation studies on ODS alloys did not consider the effect of friction stir welding but are
375 included here for context. Since welding did not introduce new phases—but mostly changed the
376 dispersoid and grain morphology—non-welded ODS alloys remain relevant. The most similar study in
377 terms of ion irradiation was performed by T. Chen et al., where MA956 was irradiated up to 180 dpa
378 measured at the ion implantation peak using 3.5 MeV Fe²⁺ [52]. At the highest dose of 145 dpa, there was
379 void swelling of ~1% reported, no voids at 325°C, and only a few isolated voids at 625°C. In another
380 study, Gelles et al. examined MA956, MA957 and HT9, T91 at 420 °C irradiated in the Fast Flux Test
381 Facility up to ~200 dpa [64]. MA956 had swelling of 1.17%, and T91 had the highest swelling of 1.76%.
382 HT9 had lower swelling: 0.09 and 1.02% in two different heat treatments. Thus, the low swelling
383 observed in this work is likely in line with other ferritic-martensitic steels and possibly more resistant to
384 void formation than other FM alloys, even after friction stir welding.

385 The largest consistent difference between the BM and SZ-M or SZ-H that is likely to affect void
386 swelling resistance is the coarsening of the grains and dispersoids. Work from other authors showed that a
387 fine grain or fine microstructure morphology promote defect trapping and annihilation [51, 59, 60], and
388 dispersoids additionally are likely to function as a site for defect recombination [51, 61, 62]. The grain
389 size increased from BM to SZ-M to SZ-H from 0.89 to 4.16 to 12.5 μm, respectively, causing sink
390 strength of the grain boundaries to decrease from $3.03 \times 10^{13} \text{ m}^{-2}$ to $1.13 \times 10^{12} \text{ m}^{-2}$ to $1.54 \times 10^{11} \text{ m}^{-2}$
391 from the BM to the SZ-M and SZ-H, respectively. However, these sink strengths are one order of
392 magnitude below the as received dispersoid sink strength ($5.98 \times 10^{13} \text{ m}^{-2}$, $6.21 \times 10^{13} \text{ m}^{-2}$, $7.16 \times 10^{12} \text{ m}^{-2}$,
393 respectively) and two orders of magnitude below the as-received dislocation network sink strength
394 ($6.14 \times 10^{13} \text{ m}^{-2}$, $6.75 \times 10^{13} \text{ m}^{-2}$, $1.84 \times 10^{14} \text{ m}^{-2}$, respectively). Getto et al. [20] provide a discussion of
395 the effect of dispersoid morphology versus sink strength comparing the BM to other ODS alloys. Their
396 results indicated that morphology (larger or smaller diameter), and not just sink strength, is related to void
397 swelling resistance, based upon the other swelling results in the ODS literature [48, 63]. It was
398 determined that the sink strength of dispersoids did not necessarily correlate with swelling resistance, but
399 a very high density of smaller dispersoids resulted in less swelling than a similar sink strength of larger,
400 less abundant dispersoids. Grain size is probably a partial contributor to the observed swelling behavior,
401 especially considering that the SZ-M often has a similar sink strength to BM but more voids formed, but
402 the dispersoid and dislocation microstructures are more likely to be controlling because of the higher sink
403 strengths.

404 To examine this, a comparison of the diameter and number density of dispersoids plotted against
405 swelling is shown in Figure 13a,b. There is a general trend with increasing diameters of dispersoids with
406 increasing swelling. Likewise, with one exception, swelling decreases weakly with increasing number
407 density. In Figure 13c, the sink strength of dispersoids is plotted against swelling. Unlike with diameter,
408 there is no clear correlation with swelling, indicating that the morphology of the precipitates is important
409 and not just the total sink strength. There was no correlation between network dislocation sink strength
410 and swelling, which is consistent with the theory offered elsewhere that network dislocations act more
411 similar to an unbiased or very low bias relative to loops [69]. However, when the total microstructure is
412 considered, including dispersoids, dislocations and grain boundaries are inversely correlated with
413 swelling (Figure 13d).

414 Thus, an ideal microstructure for void swelling resistance would more closely resemble the base
415 material with smaller, more abundant dispersoids, as opposed to fewer, larger dispersoids, and a higher
416 total sink strength from dispersoids and dislocations, but grain size as an effect cannot be totally
417 discounted. Overall, the low values of swelling despite microstructure coarsening caused by welding
418 demonstrate the excellent swelling resistance of MA956, even after welding, but with the caveat that the

419 radiation experiments performed here were with a raster scanned beam and there was no helium pre- or
420 co-injection, which would likely promote cavity nucleation [70–72].

421 4.3. Dislocations

422 Many of the trends with dislocations noted in Figure 12 and Table 4 were muted or inconsistent.
423 A potential explanation for some of this variation could be low statistics due to the difficulty of imaging
424 loops in a high sink density ferritic alloy. However, the strongest trend is that dislocation network line
425 density (Figure 12c) was larger for either welding condition compared to the BM, although the maximum
426 network density value varied between SZ-M or SZ-H. In general, the values remained consistently around
427 $\sim 2 \times 10^{14} \text{ m}^{-2}$. In similar studies on MA956 and other ODS alloys [9, 14, 55], authors observed a higher
428 dislocation density in SZ relative to the BM. The authors attributed increased dislocation density to severe
429 plastic strain from the mechanical action of the FSW tool.

430 Another finding is that loop diameter increased with temperature and dose for each of the welding
431 conditions. This is consistent with many other reports in the literature for ferritic/ferritic-martensitic
432 alloys [11, 49, 67]. An interesting outlier in the SZ-H was that the diameter decreased at the highest dose,
433 whereas BM and SZ-M were more likely to grow consistently. Interestingly, these conditions seem to
434 correlate with irradiation conditions with the largest amount of void swelling, suggesting that the voids
435 are competing for not just vacancies but also as sinks for interstitials. At 400 °C, the number density
436 tended to increase with increasing dose, especially evident in the SZ-M (Figure 12b), whereas at the
437 higher temperature, number density decreased with increasing dose after an initial spike in nucleation.
438 This is consistent with nucleation-dominant behavior at lower temperatures and more growth-dominant
439 behavior at higher temperatures [11,54].

440 In addition to variations in noted in low statistics due to difficulty of loop imaging, a recent result
441 from Kohnert et al. found a significant loss of original dislocation microstructure during sample
442 preparation by annihilation at the surface [74]. This depended on material type, slip system, and amount
443 of thinning. For the pure Fe modeled in the study, the average loss of dislocations in a thinned sample
444 between 100 and 200 nm was 40 to 30% of the bulk. Because of this large variation, thicknesses are
445 provided in Figure 11. Although approximately the same thinning and imaging procedure was followed,
446 there was some significant variation in the resulting thickness and an additional $\sim 10\%$ – 15% variation in
447 dislocation diameter, and number density caused by thickness variation may account for some of the
448 inconsistencies noted above in number density, and diameter to a lesser extent.

449 4.4. Co-evolution of the microstructure

450 The co-evolution of the irradiated microstructure is inherently a complicated combination of
451 processes to deconvolute. Thus, the approach taken in this study is to compare the sink strengths from the
452 microstructure analysis as a function of displacement damage first, then compare across irradiation
453 temperature for a fixed dose before providing a larger overview. Several common techniques are utilized
454 in subsequent paragraphs and described briefly here. Using the described sink strengths for grain
455 boundaries, dispersoids, voids, loops and the dislocation network presented in Table 3 and Table 4 as
456 inputs to Eq. (2.3) from Was [32], the rate theory model was used to calculate D_{rad} , C_i , C_v and the time
457 constants τ_1 – τ_5 described in Table 6. The time constants generally describe the onset of mutual
458 recombination (τ_1), interstitial (τ_2) or vacancy (τ_3) loss to sinks, and mutual recombination dominating
459 loss to interstitial (τ_4) and vacancy (τ_5) loss to sinks. The resulting calculations are presented in Table 7
460 and Figure 14.

461 First, for all cases, the dislocation network and loops dominate the microstructure and are
 462 expected to have the largest impact on defect behavior. For instance, the sink strength of the loops or
 463 network alone are nearly all on the order of 10^{14} m^{-2} , whereas the dispersoid sink strength remains on the
 464 order of 10^{13} m^{-2} regardless of temperature or dose. The void sink strength remained quite low, with the
 465 highest value reported for the SZ-H at 450 °C, 50 dpa of $2.6 \times 10^{13} \text{ m}^{-2}$. The sink strength generally
 466 increased with increasing dose for BM and SZ-M. The behavior in the SZ-H case was more inconsistent.
 467 Across all temperatures for SZ-H, the total sink strength at 50 dpa was larger than that at 100 or 200 dpa.
 468 This was an effect of decreasing network and loop sink strength after an initial growth period from 0 dpa
 469 as dislocations interact and coalesce. Again, some variation could be explained by the theoretical loss of
 470 dislocations during FIB sample preparation [74] already noted in Section 4.3, but as this happened at each
 471 temperature, it is likely a genuine effect.

472 Using the steady state rate theory calculations summarized in Table 7, C_v is always greater than
 473 C_i and both C_v and C_i are larger for SZ-H relative to SZ-M, regardless of temperature or dose, likely due
 474 to the of the overall lower sink strength. With increasing dose, the C_i/C_v ratio was nearly constant at a
 475 given temperature for either SZ-M or SZ-H, suggesting that the overall mechanistic behavior is
 476 dominated by a process strongly dependent on temperature rather than on the radiation damage itself. For
 477 instance, the C_i/C_v ratio for both SZ-M and SZ-H at 500 °C was ~ 0.35 even when both C_i and C_v
 478 increased in dose. With increased dose at 450 °C, the D_{rad} plateaued (SZ-H) or decreased (SZ-M) by 200
 479 dpa. Thus, the difference in response between SZ-M and SZ-H is likely controlled primarily by the
 480 thermal diffusion of point defects and solutes rather than the differing sink strengths.

481 The relative ordering of the time constants is presented in Figure 14a for SZ-M and Figure 14b
 482 for SZ-H. The time constant behavior was highly sensitive to both sink strength and temperature. At a
 483 fixed temperature of 450°C and increasing dose to determine the effect of sink strength only, for SZ-at
 484 and 50 dpa, τ_2 (interstitial loss to sinks) was the smallest followed by τ_5 (mutual recombination
 485 dominating vacancy loss to sinks). As dose increased, this behavior inverted with τ_5 the smallest followed
 486 by τ_2 at 100 and 200 dpa. The opposite behavior was observed in SZ-M (Figure 14a) where τ_2 was the
 487 smallest at 100 dpa and τ_5 was the smallest at 200 dpa. Although this may appear inconsistent, it is
 488 explained by noting that the τ_5 behavior correlated with the highest sink strength for each welded
 489 specimen, observed in the SZ-H at 50 dpa (total sink strength of $4.74 \times 10^{14} \text{ m}^{-2}$) and in SZ-M at 200 dpa
 490 (total sink strength of $6.85 \times 10^{14} \text{ m}^{-2}$), already noted above. Thus, a higher sink strength results in an
 491 earlier onset of interstitial loss to sinks and an overall higher loss of interstitials to sinks for SZ-H
 492 compared to SZ-M.

493 The overall sink strength in the BM and each FSW condition tended to decrease with increasing
 494 temperature for a given dose. The dislocation sink strength was highest at 400 °C and decreased with
 495 temperature, regardless of welding. Since dislocations dominate the microstructure in general, it is
 496 unsurprising that this is the strongest trend; it is attributed to high interstitial diffusivity at the relatively
 497 low temperature, which can nucleate and grow the loops and network, whereas the vacancies remain
 498 relatively immobile and cannot agglomerate into voids. SZ-M demonstrated these trends where the total
 499 dislocation sink strength, including loops and network, decreases from a maximum of $10.2 \pm 3.1 \times 10^{14} \text{ m}^{-2}$
 500 at 400 °C to $3.61 \pm 1.1 \times 10^{14} \text{ m}^{-2}$ at 500 °C. Dispersoid sink strength was also the lowest at 500 °C,
 501 primarily because of low number density, despite having the largest dispersoid diameter.

502 At a given dose of 100 dpa, C_v decreased with temperature for both SZ-M and SZ-H, leading to
 503 an overall increase in the C_i/C_v ratio with increasing temperature. This ratio can be thought of as
 504 representative of the relative fluxes that each feature in the microstructure experience. Indeed, D_{rad} was

505 also highly sensitive to T unlike the modest changes in D_{rad} noted with increased dose up to 200 dpa. For
 506 instance, the relative effect of increasing temperature was stronger than that of sink strength. For SZ-M,
 507 there was a 120% increase in D_{rad} from 400 to 500 °C, but the relative difference between SZ-M and SZ-
 508 H for 400 °C was only ~65% despite a decrease in sink strength of ~263%.

509 To elucidate this further, the effect of temperature on the relative ordering of time constants at a
 510 fixed dose of 100 dpa was considered in Figure 14. In the case of SZ-H (Figure 14b), τ_5 (mutual
 511 recombination dominating vacancy loss to sinks) was the shortest of the time constant at all temperatures,
 512 followed by τ_2 (interstitial loss to sinks) or τ_4 (mutual recombination dominates interstitial loss to sinks).
 513 This is because of the relatively low sink strength noted in Table 3 and Table 4 for SZ-H relative to SZ-
 514 M, allowing increased recombination with sufficient defect mobility. As a benchmark, τ_1 – τ_4 were
 515 calculated by Getto et al. [20] for BM only, and τ_5 was calculated to be lower than all values of τ_1 . τ_4
 516 except at 500 °C due to a sink strength closer to that of SZ-H rather than SZ-M, even with the order of
 517 magnitude higher grain boundary sink strength. In the case of SZ-M (Figure 14a), the behavior is more
 518 complex. At 400 and 500 °C, τ_2 is the shortest time constant. Although the total sink strength is the largest
 519 at 400 °C for 100 dpa ($10.5 \times 10^{14} \text{ m}^{-2}$); the sink strength at 500 °C is smaller than that at 450 °C ($3.35 \times$
 520 10^{14} m^{-2} and $3.94 \times 10^{14} \text{ m}^{-2}$, respectively), yet 500 °C displayed more sink dominant behavior in terms of
 521 the time constants. This is in spite of lower sink density, indicating that the increased mobility of defects
 522 at high temperature is dominant, which in turn increases the likelihood of encountering sinks. Thus, a
 523 lower sink strength can still reflect considerable vacancy, interstitial and solute mobility towards sinks,
 524 consistent with the larger diameters and increased growth dominated behavior noted in the dispersoids in
 525 Figure 9, loops in Figure 12 and voids in Table 5.

526 Therefore, the following model is proposed for the welded material. At 400 °C, ballistic
 527 dissolution and radiation-enhanced diffusion are balanced providing approximately stable dispersoid
 528 behavior. The relatively higher diffusion of interstitials promotes dislocation nucleation and growth,
 529 whereas vacancies remain relatively immobile resulting in no swelling. At 450 °C, increased radiation
 530 diffusion promotes vacancy diffusion, leading to swelling in the lower sink strength SZ-H, but only at 200
 531 dpa for BM and SZ-M. Increased recombination due to the higher D_{rad} decreases the number density of
 532 loops and total dislocation sink strength. At 500 °C, however, a further increase in the radiation-enhanced
 533 diffusion promotes growth, evidenced by larger diameters for both dispersoids (Ostwald coarsening),
 534 dislocations, and larger voids caused by the continuing higher vacancy diffusion.

535 5. Conclusions

- 536 • The dispersoid behavior in the welded material was sensitive to irradiation temperature, but a
 537 mixture of nucleation and more muted growth was observed at 400 and 450 °C, which is
 538 attributed to competing mechanisms of radiation-enhanced diffusion and Ostwald coarsening. At
 539 500 °C, growth dominated behavior is attributed to Ostwald coarsening.
- 540 • Void swelling correlated to heat input because it was much more prevalent in the welded
 541 conditions occurring at lower doses and in higher values. Overall, the low values of swelling
 542 despite microstructure coarsening caused by welding demonstrate the excellent swelling
 543 resistance of MA956, even after welding. At 450 °C, increased radiation diffusion promotes
 544 vacancy diffusion leading to swelling in the lower sink strength SZ-H—but only at high doses for
 545 BM and SZ-M. At 500 °C, the continuing higher vacancy diffusion promotes void swelling in the
 546 welded samples.
- 547 • The dislocation behavior was inconsistent, with the strongest trend being network density higher
 548 for welded versus base material and an increase in loop diameter with temperature. At lower

549 temperatures, the relatively higher diffusion of interstitials promotes dislocation nucleation and
550 growth. Increased recombination because of the higher D_{rad} decreases the number density of loops
551 and total dislocation sink strength at higher temperatures.

552 • There are two competing effects that determine whether behavior, measured by τ_2 versus τ_5 , is
553 dominated by interstitial loss to sinks instead of mutual recombination rather than loss to sinks.
554 At high temperature, regardless of welding, interstitial loss to sinks was more likely to be
555 dominant, because the radiation diffusion coefficient increased with temperature regardless of
556 welding. D_{rad} was always larger for SZ-H than SZ-M, regardless of temperature because of the
557 higher population of freely migrating vacancies.

558

559 6. Acknowledgements

560 Research supported by the Defense Threat Reduction Agency (DTRA). This work was also supported
561 by the U.S. Department of Energy, Office of Nuclear Energy under DOE Idaho Operations Office
562 Contract DE-AC07-051D14517 as part of the Nuclear Science User Facilities' Rapid Turnaround
563 Experiment program (17-906, 17-1032 and 18-1396). This paper describes objective technical results
564 and analysis. Any subjective views or opinions that might be expressed in the paper do not
565 necessarily represent the views of the U.S. Department of Energy, Department of Defense or the
566 United States Government. The authors gratefully acknowledge the MIBL staff and graduate students
567 for assistance in ion irradiation. We also thank Y. Wu for assistance at CAES and L. He, B.
568 Kombaiah and X. Liu for assistance with characterization studies performed at the MFC. The authors
569 acknowledge the Open Campus program at Army Research Laboratory in Aberdeen, MD for
570 providing access to characterization suite. Partial support for review and editing by ST sponsored by
571 the Laboratory Directed Research and Development Program of Oak Ridge National Laboratory,
572 managed by UT-Battelle, LLC, for the U. S. Department of Energy. Finally, we thank CAPT D. Ruth
573 for several insightful conversations.

574 7. Tables

575 Table 1: Composition of MA956 heat used in this research [18] determined by inductively coupled plasma mass spectrometry and LECO analysis.

Alloy	Fe	Cr	Al	Y ₂ O ₃	Ti	Mn	Si	Ni	C	Mo	S	P
MA956 (wt. %)	Bal	19.93	4.75	0.51	0.39	0.09	0.08	0.04	0.023	0.02	0.008	0.006

576

577 Table 2: Table of input parameters for calculating point defect concentrations.

Parameter	Value	Reference
Temperature, T (°C)	Input parameter	NA
Damage Rate, K ₀ (dpa/s)	Input parameter	NA
N	8.34×10^{22} at/cm ³	[43]
Lattice parameter (a)	0.288 nm	[43,75]
Sink strength	From microstructure	This work
ω_i	2.9×10^{12} s ⁻¹	[43]
ω_v	1.6×10^{13} s ⁻¹	[43]
E_m^v	0.65 eV	[76]
E_f^v	1.83 eV	[41]
E_m^i	0.35 eV	[43]
S_f	2.17k	[32]
Dislocation Bias	5%	[77]

578

579

580 Table 3: Calculated sink strength of grain boundaries, dispersoids and voids irradiated with 5 MeV Fe⁺⁺ from 400 to 500 °C up to 200 dpa. N.O. =
 581 not observed. N.E. = not examined.

Temperature (°C)	Dose (dpa)	Welding Condition	Grain Boundary Sink Strength (10 ¹⁴ m ⁻²)	Dispersoid Sink Strength (10 ¹⁴ m ⁻²)	Void Sink Strength (10 ¹⁴ m ⁻²)
RT	AR	BM	0.303	0.598	N.O.
		SZ-M	0.011	0.621	N.O.
		SZ-H	0.002	0.072	N.O.
400	50	BM	0.303	0.693	N.O.
		SZ-M	0.011	0.324	N.O.
		SZ-H	0.002	0.606	N.O.
	100	BM	0.303	0.650	N.O.
		SZ-M	0.011	0.307	N.O.
		SZ-H	0.002	0.447	N.O.
450	50	BM	0.303	0.523	N.O.
		SZ-M	N.E.	N.E.	N.E.
		SZ-H	0.002	0.971	0.260
	100	BM	0.303	0.610	N.O.
		SZ-M	0.011	0.179	N.O.
		SZ-H	0.002	0.196	0.034
	200	BM	0.303	0.599	0.003
		SZ-M	0.011	0.852	0.007
		SZ-H	0.002	0.419	0.203
500	50	BM	0.303	0.485	N.O.
		SZ-M	0.011	0.347	0.006
		SZ-H	0.002	0.170	0.011
	100	BM	0.303	0.476	N.O.
		SZ-M	0.011	0.202	0.114
		SZ-H	0.002	0.151	0.037

582 Table 4: Summary of the welded MA956 microstructure data irradiated with 5 MeV Fe⁺⁺ from 400 to 500 °C up to 200 dpa using STEM imaging.
 583 *Indicates dispersoid data was determined from EDS scans due to presence of voids. N.O.= not observed.

Experimental Conditions			Dispersoids			Dislocations					
Temperature (°C)	Dose (dpa)	Welding Condition	Number of Dispersoids	Diameter (nm)	Number Density (10 ²⁰ m ⁻³)	Number of loops	Diameter (nm)	Loop Number Density (10 ²⁰ m ⁻³)	Loop line density (10 ¹⁴ m ⁻²)	Network density (10 ¹⁴ m ⁻²)	Total Dislocation loop + network density (10 ¹⁴ m ⁻²)
RT	AR	BM	263	10.6±1.0	8.96±0.9	N.O.	N.O.	N.O.	N.O.	0.61±0.2	0.61±0.2
		SZ-M	166	18.4±1.0	5.21±0.5	N.O.	N.O.	N.O.	N.O.	1.84±0.6	1.84±0.6
		SZ-H	103	19.7±1.0	2.01±0.2	N.O.	N.O.	N.O.	N.O.	0.53±0.2	0.53±0.2
400	50	BM	373	13.2±1.0	8.35±0.8	31	27.5±1.0	10.3±2.1	1.78±0.5	1.48±0.4	3.26±1.0
		SZ-M	132	22.5±1.0	2.29±0.2	62	15.2±1.0	30.7±6.1	2.93±0.9	1.79±0.5	4.72±1.4
		SZ-H	246	19.9±1.0	4.84±0.5	54	28.0±1.0	10.6±2.1	1.87±0.6	1.51±0.5	3.38±1.0
400	100	BM	502	16.0±1.0	5.28±0.5	51	28.6±1.0	15.3±3.1	2.75±0.8	1.72±0.5	4.47±1.3
		SZ-M	45	22.0±1.0	5.43±0.5	62	23.8±1.0	49.3±9.9	7.37±2.2	2.81±0.8	10.2±3.1
		SZ-H	266	20.2±1.0	3.52±0.3	57	23.3±1.0	8.7±1.7	1.27±0.4	1.17±0.4	2.44±0.7
450	50	BM	461	13.2±1.0	6.31±0.6	31	20.1±1.0	7.3±1.5	0.93±0.3	1.53±0.5	2.45±0.7
		SZ-H*	94	23.2±1.0	4.34±0.4	53	33.5±1.0	6.2±1.2	1.3±0.4	2.47±0.7	3.77±1.1
450	100	BM	317	14.3±1.0	6.77±0.7	31	21.2±1.0	3.4±0.7	0.45±0.1	1.70±0.5	2.15±0.6
		SZ-M	98	32.8±1.0	0.87±0.09	25	18.6±1.0	18.8±4.0	2.20±0.7	0.96±0.3	3.16±0.9
		SZ-H*	56	30.4±1.0	1.03±0.1	25	48.3±1.0	1.1±0.2	0.32±0.1	1.24±0.4	1.56±0.5
	200	BM	190	15.4±1.0	6.19±0.6	31	37.9±1.0	13.8±2.8	3.29±1.0	1.44±0.4	4.73±1.4
		SZ-M*	212	18.4±1.0	7.37±0.7	26	35.6±1.0	16.8±3.4	3.76±1.1	2.23±0.7	5.99±1.8
		SZ-H*	66	28.3±1.0	2.36±0.2	29	23.4±1.0	3.6±0.7	0.53±0.2	1.49±0.4	2.02±0.6
500	50	BM	335	13.0±1.0	5.93±0.6	38	40.8±1.0	8.3±1.7	2.14±0.6	1.31±0.4	3.45±1.0
		SZ-M*	90	24.8±1.0	2.24±0.2	55	29.6±1.0	20.1±4.0	3.73±1.1	1.47±0.4	5.20±1.6
		SZ-H*	43	22.0±1.0	1.23±0.1	32	51.8±1.0	7.8±1.6	2.55±0.8	2.46±0.7	5.01±1.5
	100	BM	279	16.7±1.0	4.53±0.5	33	93.4±1.0	4.7±0.9	2.73±0.8	1.45±0.4	4.18±1.3
		SZ-M*	69	25.1±1.0	1.28±0.1	60	52.7±1.0	6.3±1.3	2.09±0.6	1.52±0.5	3.61±1.1
		SZ-H*	40	32.2±1.0	0.74±0.07	20	33.6±1.0	8.7±1.7	1.75±0.5	0.83±0.2	2.63±0.8

584

585 Table 5: Void data determined from EDS composition scans of welded MA956 irradiated with 5 MeV Fe⁺⁺ from 400 to 500 °C up to 200 dpa.
 586 N.O.= not observed.

Welding Conditions	Temperature (°C)	Dose (dpa)	Number of Voids	Diameter (nm)	Number Density (10 ²⁰ m ⁻³)	Swelling (%)
BM	450	200	1	14.4	0.0345	0.0005%
SZ-M	400	50	0	N.O.	N.O.	N.O.
		100	0	N.O.	N.O.	N.O.
	450	50	0	N.O.	N.O.	N.O.
		100	0	N.O.	N.O.	N.O.
		200	5	6.7	0.174	0.0004%
	500	50	1	35.8	0.0248	0.01%
100		37	26.5	0.687	0.11%	
SZ-H	400	50	0	N.O.	N.O.	N.O.
		100	0	N.O.	N.O.	N.O.
	450	50	31	15.2	2.72	0.07%
		100	5	59.0	0.0917	0.16%
		200	23	39.3	0.822	0.50%
	500	50	2	31.8	0.0573	0.01%
100		6	52.7	0.112	0.15%	

587

588

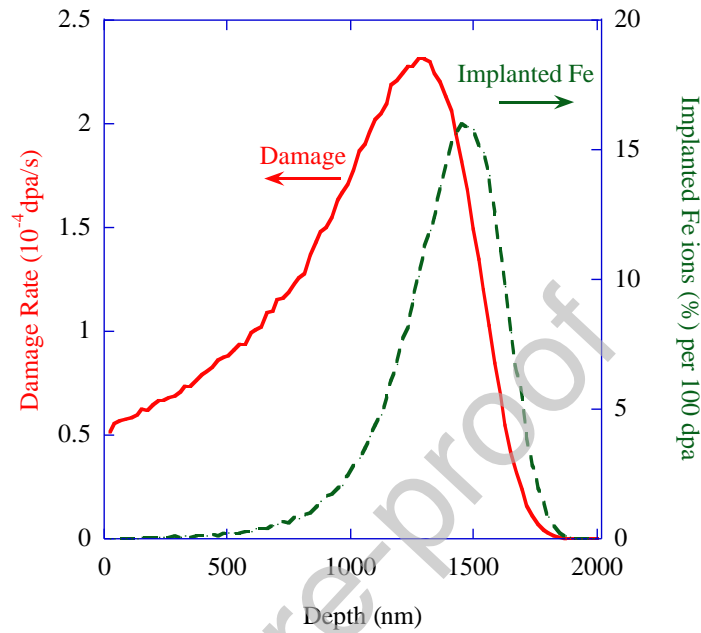
589 Table 6: Time constants in the point defect balance equations for the rate-limiting processes. Adapted from [32].

Time constant	Value	Process
τ_1	$(K_0 K_{iv})^{-\frac{1}{2}}$	Onset of mutual recombination
τ_2	$(K_{is} C_s)^{-1}$	Onset of interstitial loss to sinks
τ_3	$(K_{vs} C_s)^{-1}$	Onset of vacancy loss to sinks
τ_4	$\frac{K_{is} C_s}{K_0 K_{iv}}$	Mutual recombination dominates interstitial loss to sinks
τ_5	$\frac{K_{vs} C_s}{K_0 K_{iv}}$	Mutual recombination dominates vacancy loss to sinks

590 Table 7: Results from rate theory model at 100 dpa and from 50 to 100 dpa at 450°C. Values for BM repeated here from [20] to provide context.
 591 N.E. = not examined.

Temperature (°C)	Dose (dpa)	Welding Conditions	$C_i (\times 10^6)$	$C_v (\times 10^6)$	$\tau_1 (\times 10^{-4} \text{s})$	$\tau_2 (\times 10^{-4} \text{s})$	$\tau_3 (\times 10^{-4} \text{s})$	$\tau_4 (\times 10^{-4} \text{s})$	$\tau_5 (\times 10^{-4} \text{s})$	$D_{\text{rad}} (\times 10^{16} \text{m}^2/\text{s})$
400	100	BM	1.00	5.51	0.35	0.19	1.03	0.66	0.13	1.93
		SZ-M	0.71	3.99	0.35	0.10	0.53	1.30	0.23	1.39
		SZ-H	1.19	6.59	0.35	0.35	1.94	0.35	0.06	2.31
450	50	BM	0.86	3.31	0.31	0.20	0.79	0.46	0.12	2.52
		SZ-M	N.E.	N.E.	N.E.	N.E.	N.E.	N.E.	N.E.	N.E.
		SZ-H	0.71	2.76	0.31	0.13	0.52	0.70	0.18	2.11
	100	BM	0.87	3.35	0.31	0.22	0.84	0.44	0.17	2.55
		SZ-M	0.83	3.25	0.31	0.20	0.77	0.48	0.12	2.47
		SZ-H	1.00	3.88	0.31	0.37	1.44	0.26	0.07	2.94
	200	BM	0.75	2.93	0.28	0.12	0.46	0.68	0.18	2.23
		SZ-M	0.77	2.62	0.28	0.10	0.38	0.83	0.21	1.99
		SZ-H	1.01	3.93	0.28	0.25	0.98	0.32	0.08	2.99
500	100	BM	0.64	1.82	0.23	0.009	0.27	0.56	0.21	2.71
		SZ-M	0.72	2.06	0.23	0.12	0.33	0.45	0.16	3.07
		SZ-H	0.85	2.44	0.23	0.17	0.49	0.30	0.11	3.64

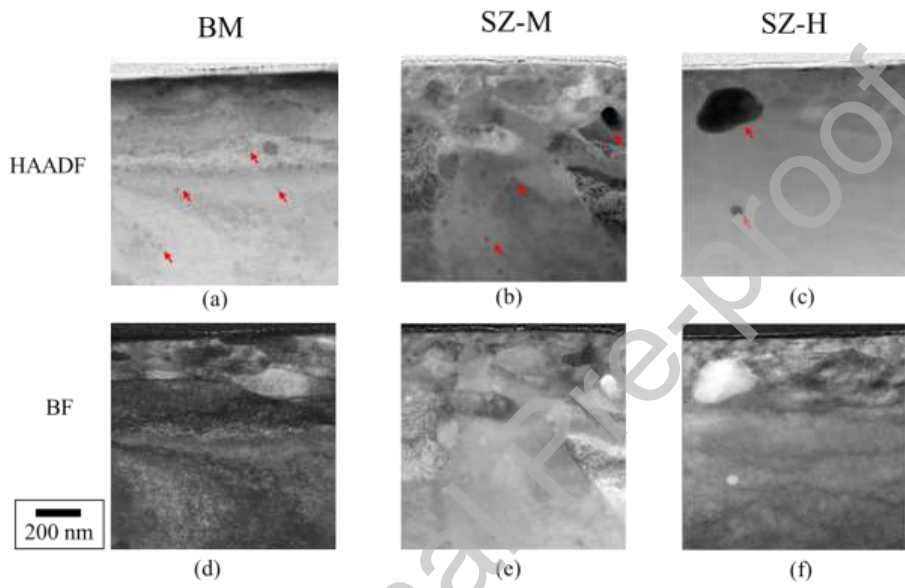
592 8. Figures



593

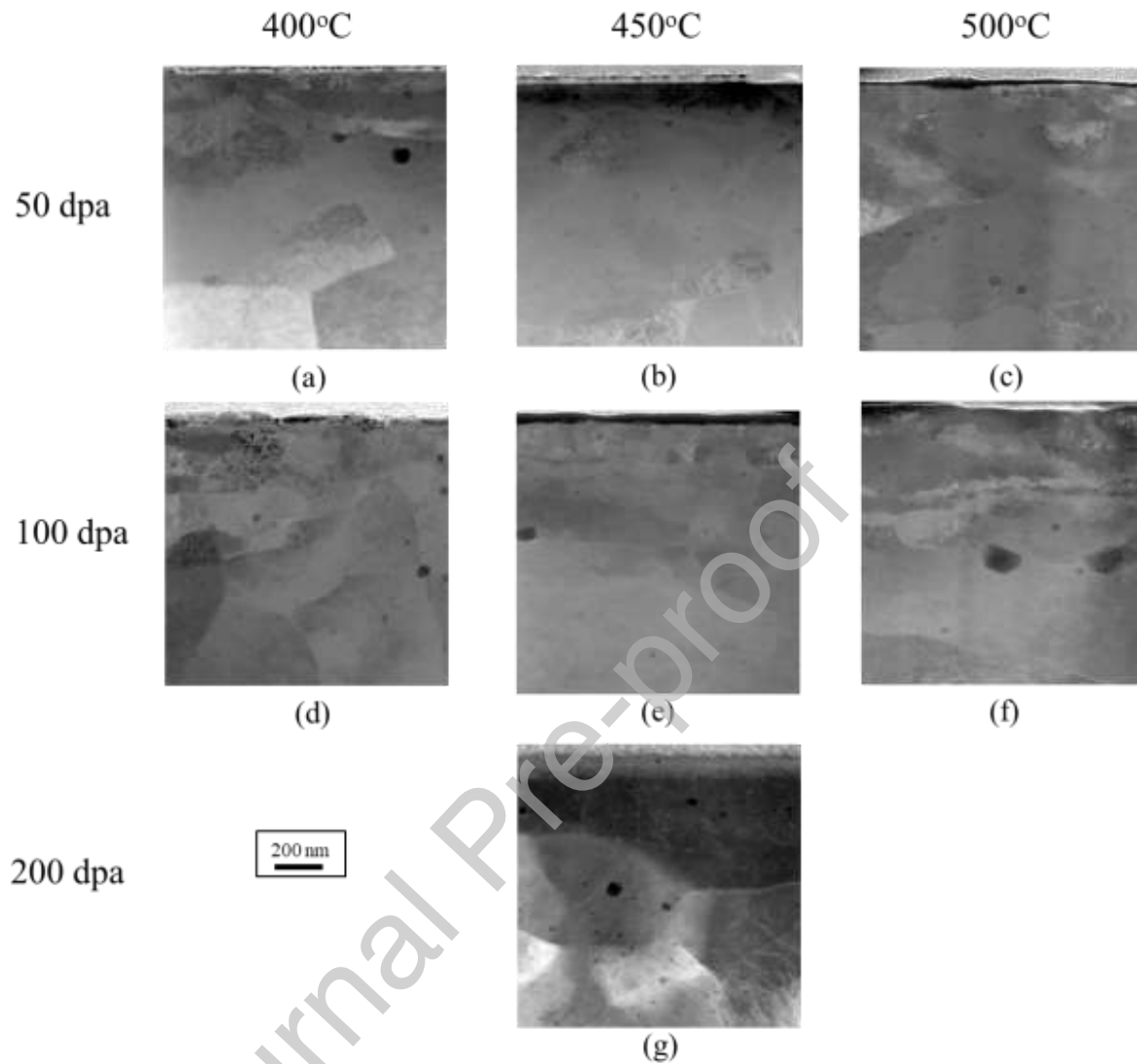
594 Figure 1: The damage rate (red solid) is overlaid upon the implanted ion concentration (green dashed) for
595 5 MeV Fe⁺⁺ in Fe-19Cr.

596



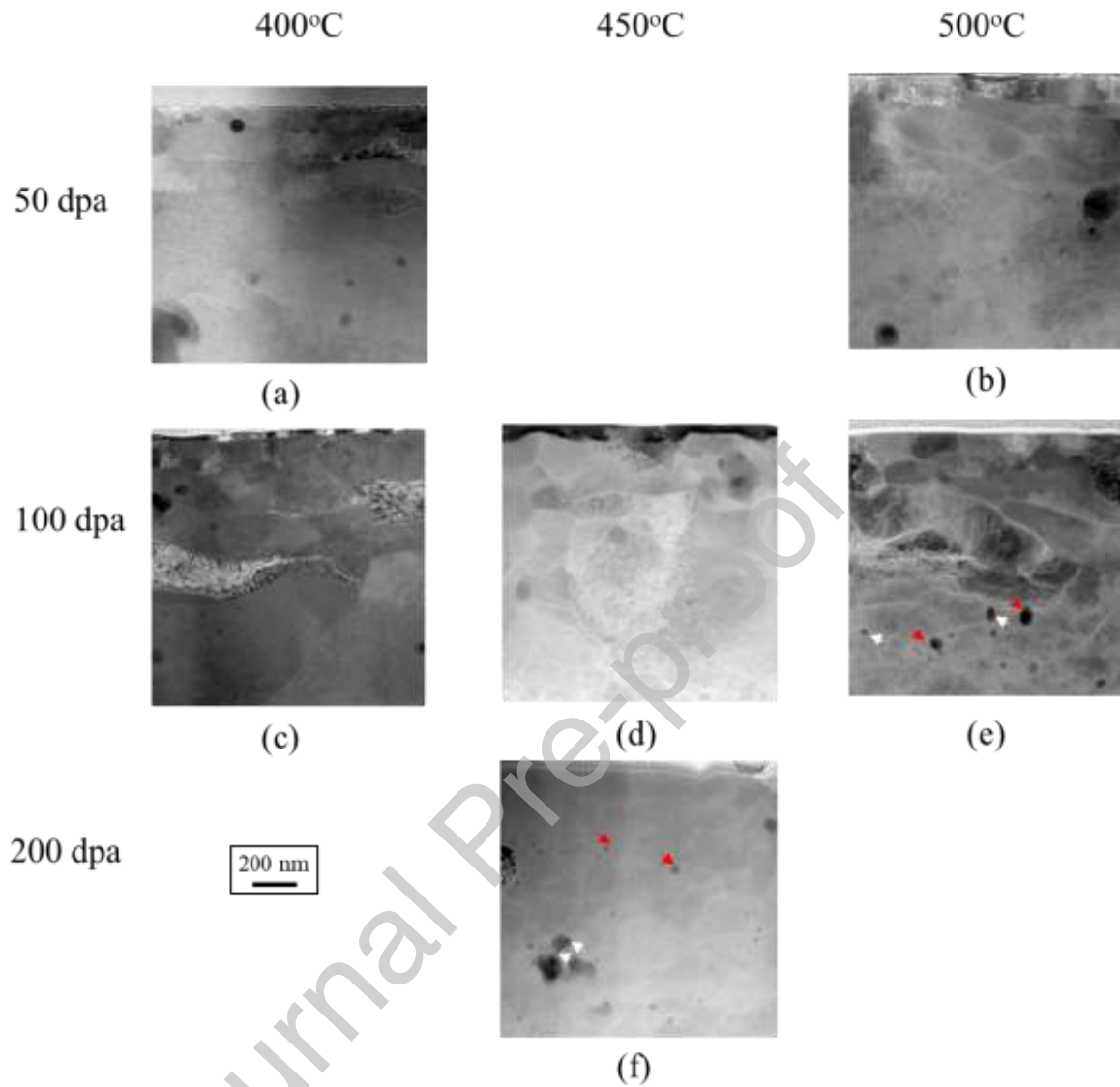
597

598 Figure 2: HADDF (a–c) and BF (d–f) images of the as received BM, SZ-M and SZ-H. BM and SZ-H reprinted from [13] with permission. Red
599 arrows point to select dispersoids.



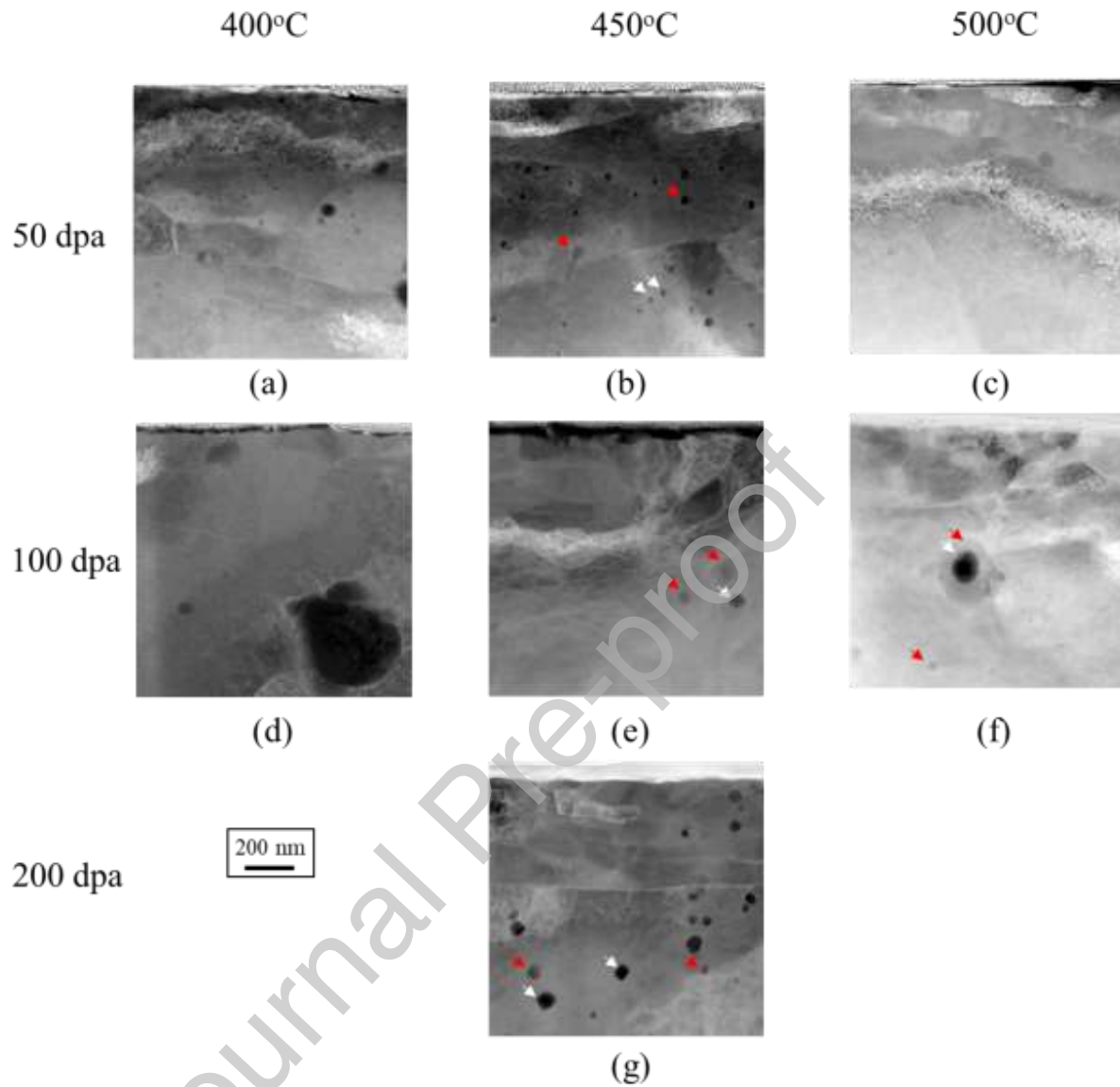
600

601 Figure 3: HAADF images of MA956 base material (BM) irradiated with 5 MeV Fe⁺⁺ from 400 to 500 °C
602 up to 200 dpa. Reprinted with permission from Getto et al. [20].



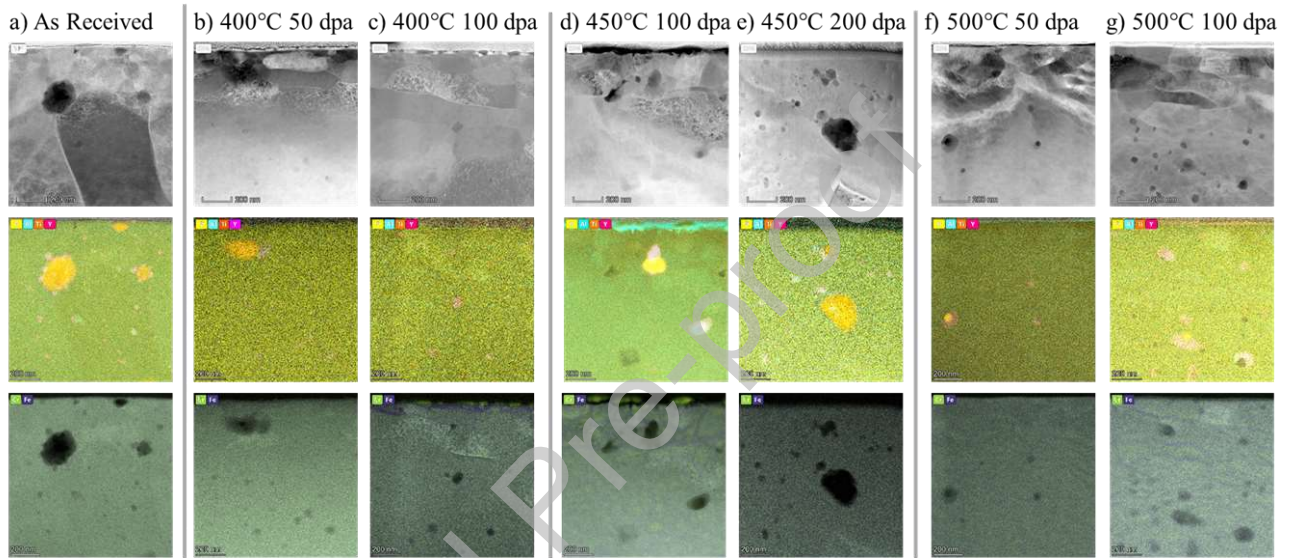
603

604 Figure 4: HAADF images of MA956 friction stir welded with medium heat input (SZ-M) and irradiated
605 with 5 MeV Fe⁺⁺ from 400 to 500 °C up to 200 dpa.



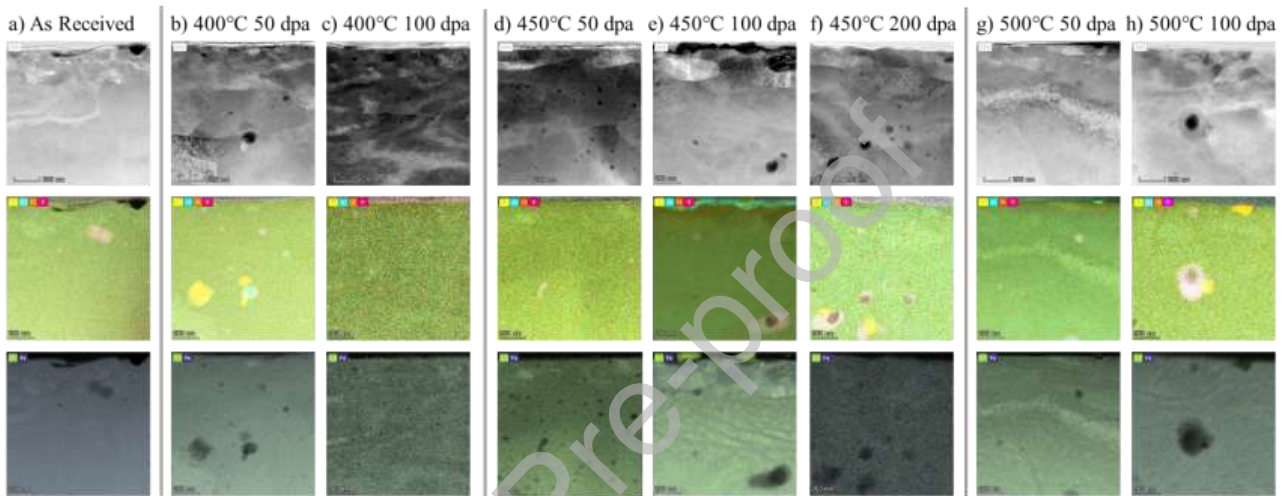
606

607 Figure 5: HAADF images of MA956 friction stir welded with high heat input (SZ-H) and irradiated with
608 5 MeV Fe^{++} from 400 to 500 °C up to 200 dpa.



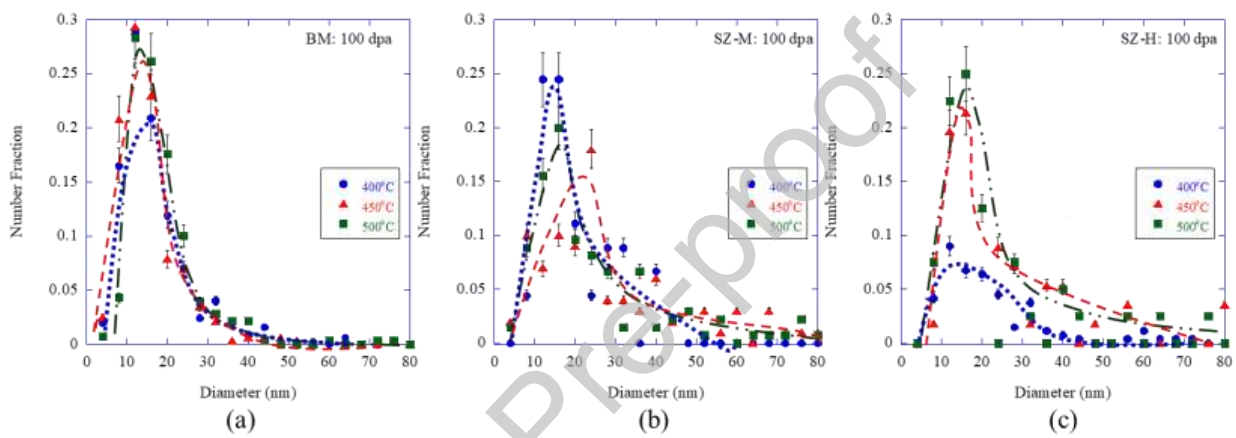
609

610 Figure 6: EDS composition scans and corresponding HAADF images for SZ-M irradiated with 5 MeV Fe⁺⁺ from 400 to 500 °C up to 200 dpa.



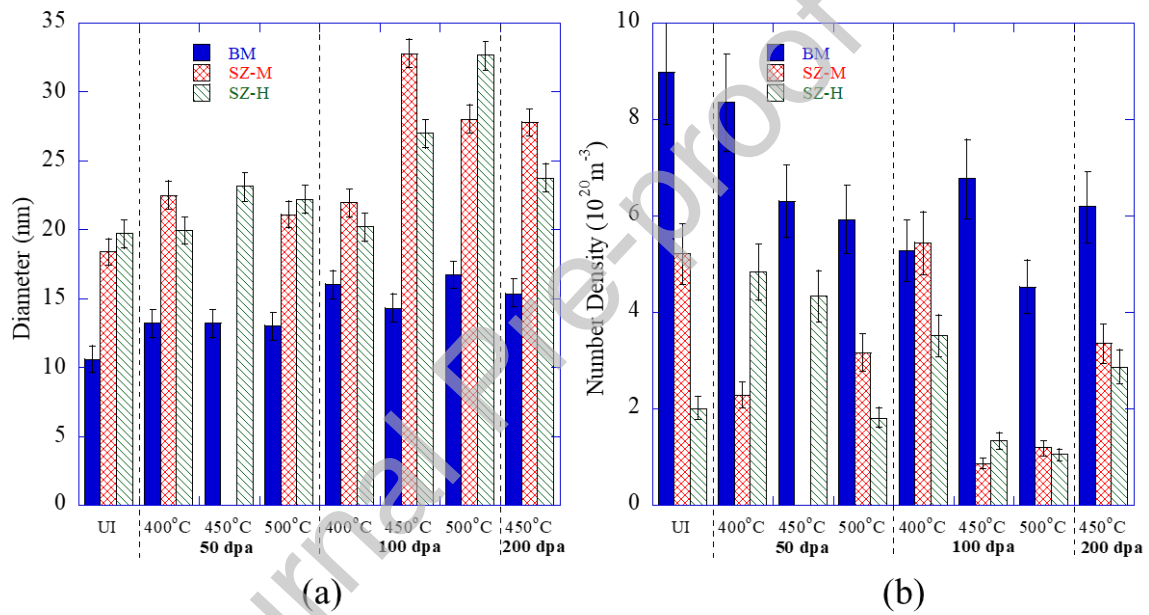
611

612 Figure 7: EDS composition scans and corresponding HAADF images for SZ-H irradiated with 5 MeV Fe⁺⁺ from 400 to 500 °C up to 200 dpa.



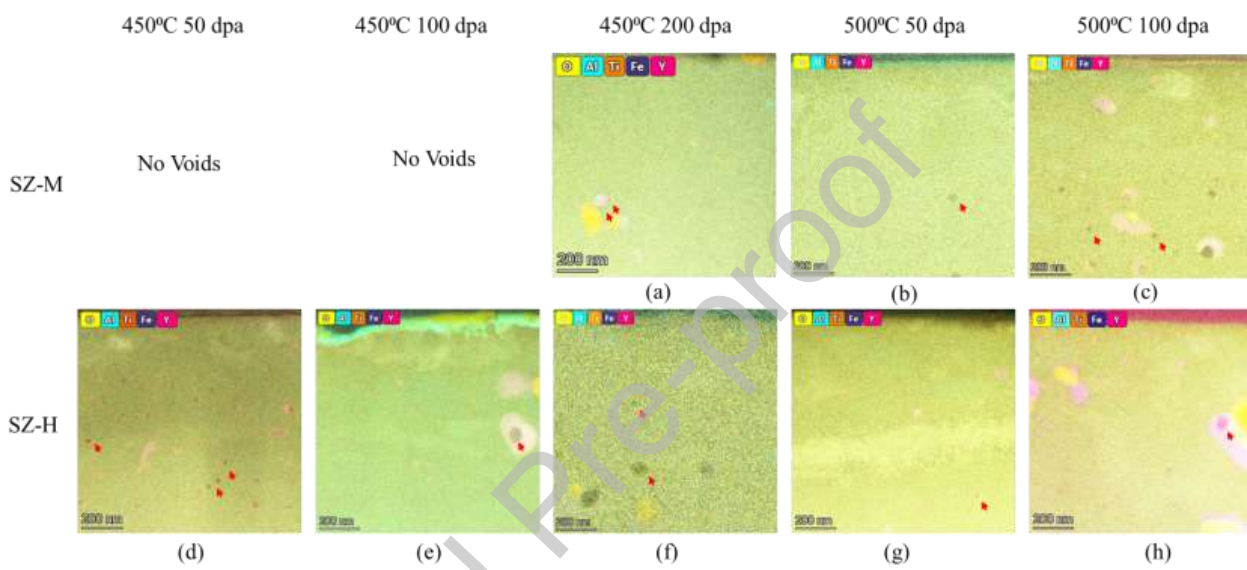
613

614 Figure 8: Diameter distribution for dispersoids measured via HAADF imaging at 100 dpa for (a) BM, (b) SZ-M and (c) SZ-H. Distribution are
 615 limited to 80 nm for ease of viewing. For experimental conditions with voids, the dispersoid distributions were taken from the ChemiSTEM
 616 images. Lines guides the eye.



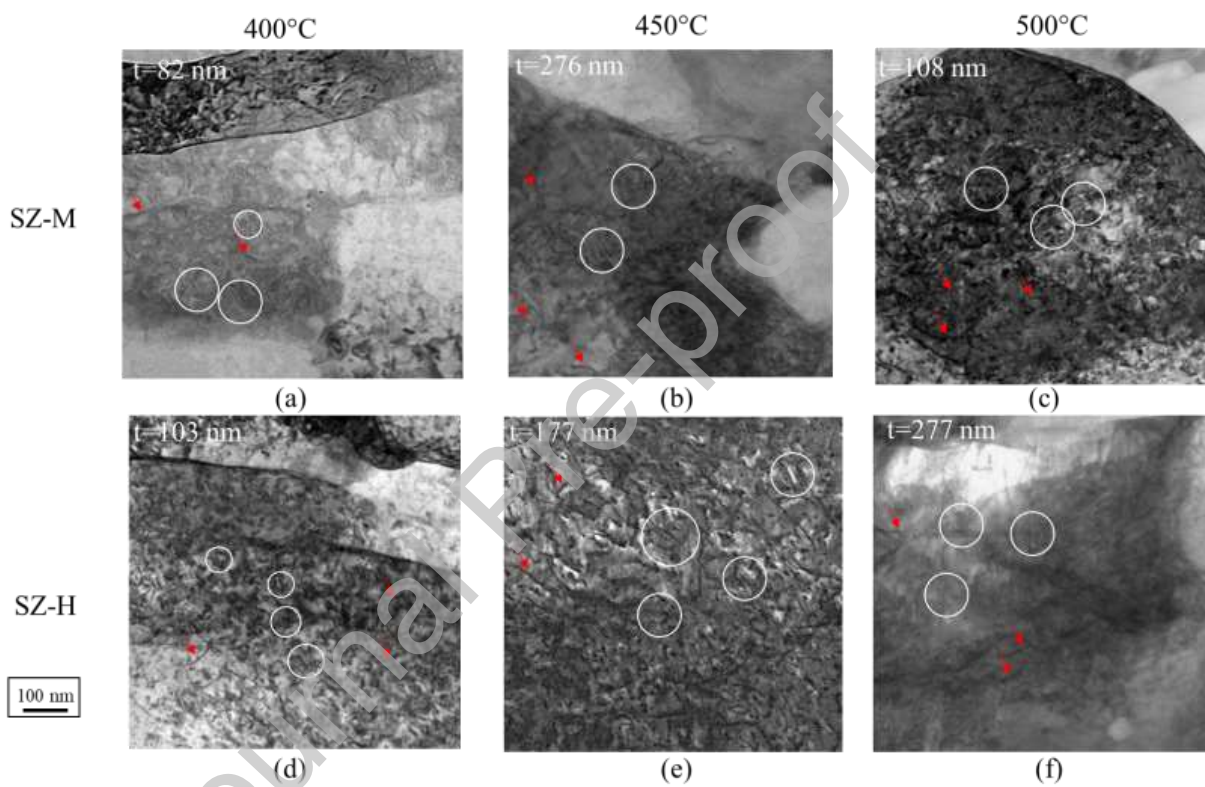
617

618 Figure 9: Dispersoid (a) diameter and (b) number density as function of dose at 400 °C, 450 °C, and 500 °C for ion irradiated friction stir welded
 619 MA956. EDS scans used for characterization of dispersoids in experimental conditions with voids.



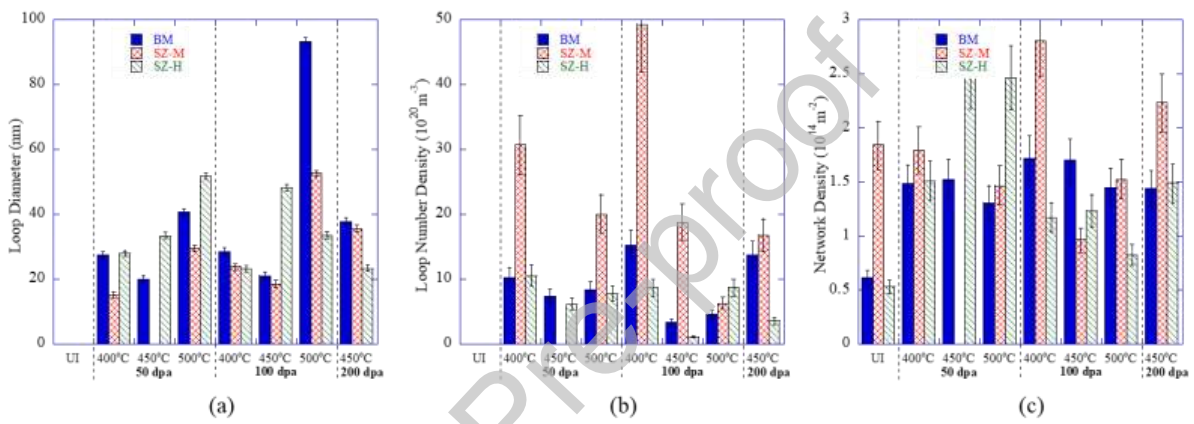
620

621 Figure 10: EDS scans with O, Al, Ti, Fe and Y shown for cases where void swelling occurred in SZ-M and SZ-H. Voids are identified from the
 622 dark areas, which are depleted in all elements. Examples of selected voids are marked with red arrows. Note that these are intensity maps and
 623 colors are adjusted for ease of imaging.



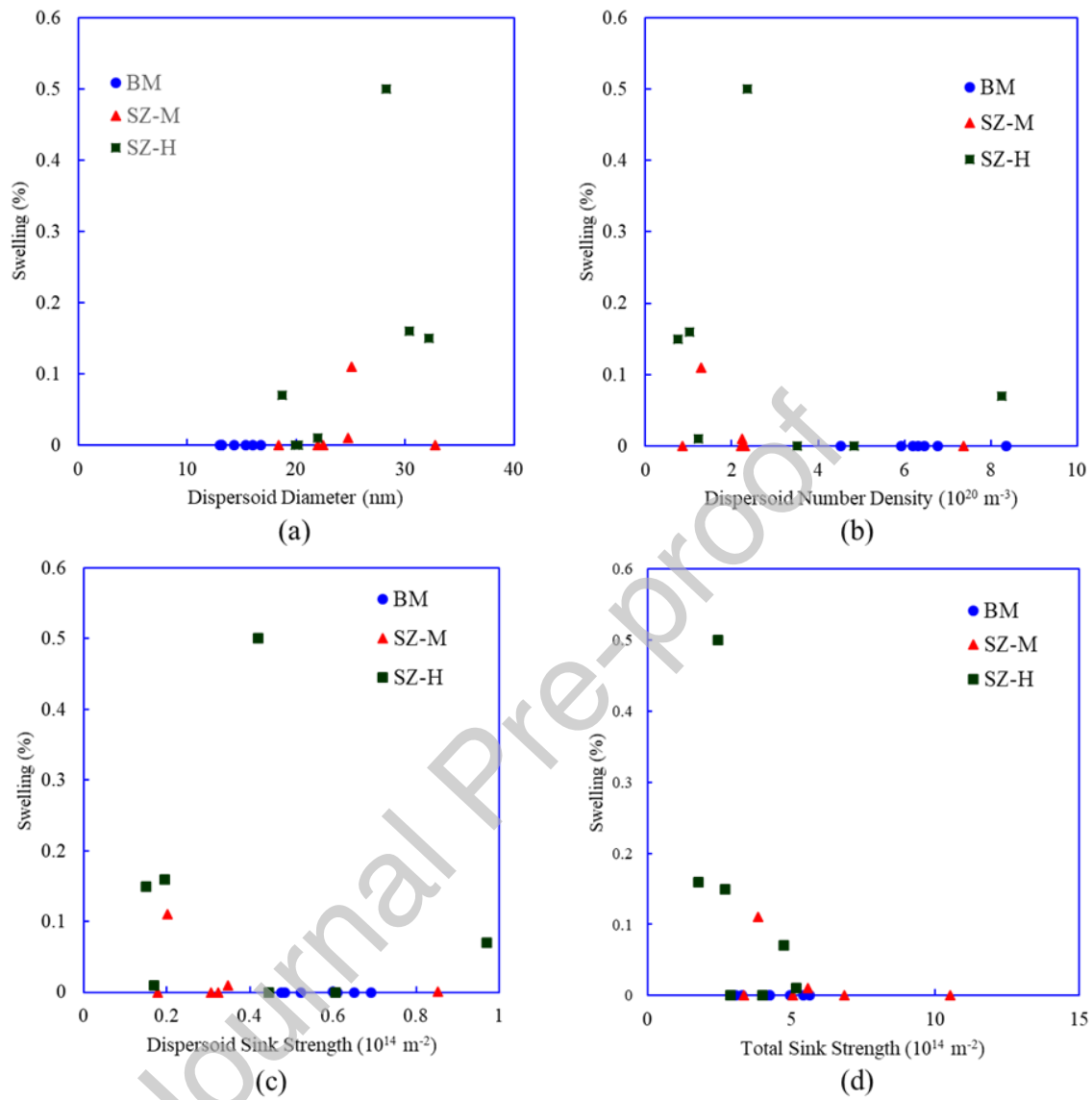
624

625 Figure 11: Selected BF images of SZ-M and SZ-H for loop analysis at 100 dpa with 5 MeV Fe^{++} . The SZ-M samples are shown in (a)-(c) and the
 626 SZ-H are shown in (d)-(f). Selected loops are marked by white circles whereas selected network lines are marked by red arrows. The thickness
 627 values for each image are shown in the top left corner.



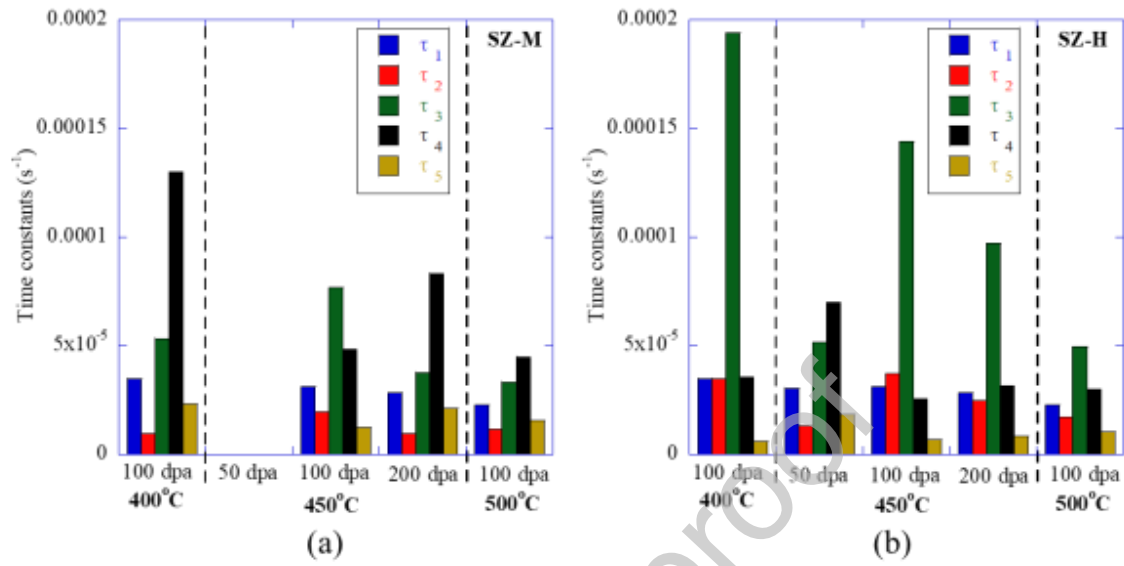
628

629 Figure 12: Loop (a) diameter (b) number density and (c) network line density in welded MA956 irradiated with 5 MeV Fe⁺⁺.



630

631 Figure 13: Void swelling plotted as a function of (a) dispersoid diameter (b) dispersoid number density
 632 (c) dispersoid sink strength and (d) total sink strength.



633

634 Figure 14: Results from rate theory model at 100 dpa and from 50 to 100 dpa at 450 °C for a) SZ-M and
 635 b) SZ-H.

636 **Declaration of interests**

637

- 638 9. The authors declare that they have no known competing financial interests or personal
 639 relationships that could have appeared to influence the work reported in this paper.

640

641 **CRedit Author statement**

642 Elizabeth Getto: Project administration, Methodology, Investigation, Formal Analysis, Visualization,
 643 Writing—Original Draft, Supervision, Funding acquisition

644 Nicholas Nathan: Investigation, Writing—Review & Editing

645 Jack McMahan: Investigation, Writing—Review & Editing

646 Stephen Taller: Conceptualization, Methodology, Software, Writing—Review & Editing

647 Brad Baker: Conceptualization, Resources, Writing—Review & Editing, Funding acquisition

648

649

650

651 **10. References**

- 652 [1] W.M. Gajewski, H. Esselman, B. Wolfe, J.J. Taylor, FFTF, Companion test and development
 653 facility for the LMFBR program, ASME Meet. (1971).
- 654 [2] C.R.F. Azevedo, Selection of fuel cladding material for nuclear fission reactors, *Eng. Fail. Anal.*
 655 18 (2011) 1943–1962. doi:10.1016/j.engfailanal.2011.06.010.
- 656 [3] B.W. Baker, E.S.K. Menon, T.R. McNelley, L.N. Brewer, B. El-Dasher, J.C. Farmer, S.G. Torres,
 657 M.W. Mahoney, S. Sanderson, Processing-Microstructure Relationships in Friction Stir Welding
 658 of MA956 Oxide Dispersion Strengthened Steel, *Metall. Mater. Trans. E. 1* (2014) 318–330.
 659 doi:10.1007/s40553-014-0033-6.
- 660 [4] R.S. Mishra, Z.Y. Ma, Friction stir welding and processing, *Mater. Sci. Eng. R Reports.* 50 (2005)
 661 1–78. doi:10.1016/j.mser.2005.07.001.
- 662 [5] B.W. Baker, L.N. Brewer, Joining of Oxide Dispersion Strengthened Steels for Advanced
 663 Reactors, *JOM.* 66 (2014) 2442–2457. doi:10.1007/s11837-014-1206-6.
- 664 [6] Z. Yu, Z. Feng, D. Hoelzer, L. Tan, M.A. Sokolov, Friction Stir Welding of ODS and RAFM
 665 Steels, *Metall. Mater. Trans. E. 2* (2015) 164–172. doi:10.1007/s40553-015-0054-9.
- 666 [7] B. Jasthi, S. Howard, W. Arbegast, G. Grant, S. Koduri, D. Herling, Friction Stir Welding of MA
 667 957 Oxide Dispersion Strengthened Ferritic Steel, in: *Frict. Stir Weld. Process. III, 2005: pp. 75–*
 668 *79.*
- 669 [8] Q. Wu, M. Li, Y. Guo, J. Shan, H. Wang, Y. Chang, Microstructural evolution and mechanical
 670 properties of friction stir welded 12Cr-ODS steel, *Nucl. Mater. Energy.* 25 (2020).
 671 doi:10.1016/j.nme.2020.100804.
- 672 [9] J. Wang, W. Yuan, R.S. Mishra, I. Charit, Microstructure and mechanical properties of friction stir
 673 welded oxide dispersion strengthened alloy, *J. Nucl. Mater.* 432 (2013) 274–280.
 674 doi:10.1016/j.jnucmat.2012.08.001.
- 675 [10] G.S. Was, Z. Jiao, E. Getto, K. Sun, A.M. Monterrosa, S.A. Maloy, O. Anderoglu, B.H. Sencer,
 676 M. Hackett, Emulation of reactor irradiation damage using ion beams, *Scr. Mater.* 88 (2014) 33–

- 677 36. doi:10.1016/j.scriptamat.2014.06.003.
- 678 [11] S. Taller, Z. Jiao, K. Field, G.S. Was, Emulation of fast reactor irradiated T91 using dual ion beam
679 irradiation, *J. Nucl. Mater.* 527 (2019). doi:10.1016/j.jnucmat.2019.151831.
- 680 [12] E. Getto, G. Vancoervering, G.S. Was, The co-evolution of microstructure features in self-ion
681 irradiated HT9 at very high damage levels, *J. Nucl. Mater.* 484 (2017) 193–208.
682 doi:10.1016/j.jnucmat.2016.12.006.
- 683 [13] E. Getto, B. Baker, B. Tobie, S. Briggs, K. Hattar, K. Knipling, Effect of friction stir welding and
684 self-ion irradiation on dispersoid evolution in oxide dispersion strengthened steel MA956 up to 25
685 dpa, *J. Nucl. Mater.* 515 (2019) 407–419. doi:10.1016/j.jnucmat.2018.12.040.
- 686 [14] Y.H. Guo, Y.Q. Chang, J. Zhang, J.Z. Li, S. Ukai, F.R. Wan, Microstructures and ion-irradiation
687 behaviour of friction stir welded 12Cr-ODS steel, *Sci. Technol. Weld. Join.* 23 (2018) 50–57.
688 doi:10.1080/13621718.2017.1392075.
- 689 [15] C.L. Chen, A. Richter, R. Kögler, L.T. Wu, Dual-beam irradiation of friction stir spot welding of
690 nanostructured ferritic oxide dispersion strengthened alloy, *J. Alloys Compd.* 536 (2012) S194–
691 S199. doi:10.1016/j.jallcom.2011.11.055.
- 692 [16] C.L. Chen, A. Richter, R. Kögler, M. Griepentrog, P. Reinstädt, Ion-irradiation effects on
693 dissimilar friction stir welded joints between ODS alloy and ferritic stainless steel, *J. Alloys
694 Compd.* 615 (2015) S448–S453. doi:10.1016/j.jallcom.2013.11.123.
- 695 [17] B.W. Baker, K.E. Knipling, L.N. Brewer, Oxide Particle Growth During Friction Stir Welding of
696 Fine Grain MA956 Oxide Dispersion-Strengthened Steel, *Metall. Mater. Trans. E.* 4 (2017) 1–12.
697 doi:10.1007/s40553-016-0101-1.
- 698 [18] B.W. Baker, T.R. McNelley, L.N. Brewer, Grain size and particle dispersion effects on the tensile
699 behavior of friction stir welded MA956 oxide dispersion strengthened steel from low to elevated
700 temperatures, *Mater. Sci. Eng. A.* 589 (2014) 217–227. doi:10.1016/j.msea.2013.09.092.
- 701 [19] B.W. Baker, Processing, Microstructure, and Material Property Relationships Following Friction
702 Stir Welding of Oxide Dispersion Strengthened Steels (Doctoral Dissertation, Naval Postgraduate
703 School, Monterey, CA), (2013).
- 704 [20] E. Getto, N. Nathan, J. McMahan, B. Baker, S. Taller, Contextualizing dispersoid evolution within
705 the microstructure of MA956 using ion irradiation, *Nucl. Mater. Energy.* 28 (2021) 101024.
706 doi:10.1016/j.nme.2021.101024.
- 707 [21] J.F. Ziegler, M.D. Ziegler, J.P. Biersack, SRIM - The stopping and range of ions in matter (2010),
708 *Nucl. Instruments Methods Phys. Res. Sect. B Beam Interact. with Mater. Atoms.* 268 (2010)
709 1818–1823. doi:10.1016/j.nimb.2010.02.091.
- 710 [22] L.A. Giannuzzi, J.L. Drown, S.R. Brown, R.B. Irwin, F. Stevie, Applications of the FIB lift-out
711 technique for TEM specimen preparation, *Microsc Res Tech.* 41 (1998) 285–290. doi:10.1055/s-
712 0033-1341065.
- 713 [23] T. Malis, S.C. Cheng, R.F. Egerton, EELS log-ratio technique for specimen-thickness
714 measurement in the TEM, *J. Electron Microsc. Tech.* 193–200 (1988).
- 715 [24] E. Getto, Z. Jiao, A.M. Monterrosa, K. Sun, G.S. Was, Effect of pre-implanted helium on void
716 swelling evolution in self-ion irradiated HT9, *J. Nucl. Mater.* 462 (2015) 458–469.
717 doi:10.1016/j.jnucmat.2015.01.045.
- 718 [25] D.B. Williams, C.B. Carter, *Transmission Electron Microscopy*, 2009.
- 719 [26] D.B. Williams, C.B. Carter, *Phase-Contrast Images*, in: *Transm. Electron Microsc.*, Springer US,
720 Boston, MA, 2009: pp. 389–405. doi:10.1007/978-0-387-76501-3_23.
- 721 [27] C.M. Parish, K.G. Field, A.G. Certain, J.P. Wharry, Application of STEM characterization for
722 investigating radiation effects in BCC Fe-based alloys, *J. Mater. Res.* 30 (2015) 1275–1289.
723 doi:10.1557/jmr.2015.32.
- 724 [28] C.M. Parish, K.G. Field, A.G. Certain, J.P. Wharry, Application of STEM characterization for
725 investigating radiation effects in BCC Fe-based alloys, *J. Mater. Res.* 30 (2015) 1275–1289.
726 doi:10.1557/jmr.2015.32.

- 727 [29] C.S. Smith, L. Guttman, Smith and Guttman--Measurement of internal boundaries in 3D structures
728 by random sectioning.pdf, *J. Met. Trans. AIME*. 5 (1953) 81–87.
- 729 [30] C. Xu, In-Situ Proton Irradiation Creep of FM Steel T91 (Doctoral dissertation, University of
730 Michigan, Ann Arbor, MI), (2014).
- 731 [31] E. Getto, An Experimental and Rate Theory Model for Understanding the Radiation Effects in
732 Friction Stir Welded MA956 Ion Irradiation, *Mendeley Data*, V1. (2021) 17632.
733 doi:10.17632/gghs8zh2dw.1.
- 734 [32] G.S. Was, *Fundamentals of Radiation Materials Science*, 2007. doi:10.1016/b978-0-12-803581-
735 8.00668-8.
- 736 [33] K.G. Field, L.M. Barnard, C.M. Parish, J.T. Busby, D. Morgan, T.R. Allen, Dependence on grain
737 boundary structure of radiation induced segregation in a 9 wt.% Cr model ferritic/martensitic steel,
738 *J. Nucl. Mater.* 435 (2013) 172–180. doi:10.1016/j.jnucmat.2012.12.026.
- 739 [34] T.S. Duh, J.J. Kai, F.R. Chen, L.H. Wang, Effects of grain boundary misorientation on the solute
740 segregation in austenitic stainless steels, *J. Nucl. Mater.* 258–263 (1998) 2064–2068.
741 doi:10.1016/S0022-3115(98)00124-X.
- 742 [35] A.A. Kohnert, M.A. Cusentino, B.D. Wirth, Molecular statics calculations of the biases and point
743 defect capture volumes of small cavities, *J. Nucl. Mater.* 499 (2018) 480–489.
744 doi:10.1016/j.jnucmat.2017.12.005.
- 745 [36] W.G. Wolfer, M. Ashkin, Stress-induced diffusion of point defects to voids, *Scr. Metall.* 7 (1973)
746 1175–1180.
- 747 [37] M.L. Lescoat, J. Ribis, A. Gentils, O. Kaïtasov, Y. De Carlan, A. Legris, In situ TEM study of the
748 stability of nano-oxides in ODS steels under ion-irradiation, *J. Nucl. Mater.* 428 (2012) 176–182.
749 doi:10.1016/j.jnucmat.2011.12.009.
- 750 [38] C. Hin, B.D. Wirth, Formation of Y₂O₃ nanoclusters in nano-structured ferritic alloys: Modeling
751 of precipitation kinetics and yield strength, *J. Nucl. Mater.* 402 (2010) 30–37.
752 doi:10.1016/j.jnucmat.2010.04.020.
- 753 [39] G.F. Knoll, *Radiation Detection and Measurement*, Third Edition, 2000. doi:10.1002/hep.22108.
- 754 [40] F. Soisson, C.C. Fu, Cu-precipitation kinetics in α -Fe from atomistic simulations: Vacancy-
755 trapping effects and Cu-cluster mobility, *Phys. Rev. B - Condens. Matter Mater. Phys.* 76 (2007)
756 1–12. doi:10.1103/PhysRevB.76.214102.
- 757 [41] E. Del Rio, J.M. Sampedro, H. Dogo, M.J. Caturla, M. Caro, A. Caro, J.M. Perlado, Formation
758 energy of vacancies in FeCr alloys: Dependence on Cr concentration, *J. Nucl. Mater.* 408 (2011)
759 18–24. doi:10.1016/j.jnucmat.2010.10.021.
- 760 [42] J. Ribis, M.L. Lescoat, Y. De Carlan, J.M. Costantini, I. Monnet, T. Cozzika, F. Delabrouille, J.
761 Malaplate, Stability of nano-oxides upon heavy ion irradiation of an ODS material, *J. Nucl. Mater.*
762 417 (2011) 262–265. doi:10.1016/j.jnucmat.2010.12.068.
- 763 [43] J.P. Wharry, G.S. Was, The mechanism of radiation-induced segregation in ferritic-martensitic
764 alloys, *Acta Mater.* 65 (2014) 42–55. doi:10.1016/j.actamat.2013.09.049.
- 765 [44] J.P. Wharry, M.J. Swenson, K.H. Yano, A review of the irradiation evolution of dispersed oxide
766 nanoparticles in the b.c.c. Fe-Cr system: Current understanding and future directions, *J. Nucl.*
767 *Mater.* 486 (2017) 11–20. doi:10.1016/j.jnucmat.2017.01.009.
- 768 [45] T.R. Allen, J. Gan, J.I. Cole, M.K. Miller, J.T. Busby, S. Shutthanandan, S. Thevuthasan,
769 Radiation response of a 9 chromium oxide dispersion strengthened steel to heavy ion irradiation, *J.*
770 *Nucl. Mater.* 375 (2008) 26–37. doi:10.1016/j.jnucmat.2007.11.001.
- 771 [46] P. Dubuisson, D. Gilbon, J.L. Séran, Microstructural evolution of ferritic-martensitic steels
772 irradiated in the fast breeder reactor Phénix, *J. Nucl. Mater.* 205 (1993) 178–189.
773 doi:10.1016/0022-3115(93)90080-I.
- 774 [47] K.H. Heinig, T. Müller, B. Schmidt, M. Strobel, W. Möller, Interfaces under ion irradiation:
775 Growth and taming of nanostructures, *Appl. Phys. A Mater. Sci. Process.* 77 (2003) 17–25.
776 doi:10.1007/s00339-002-2061-9.

- 777 [48] M.L. Lescoat, J. Ribis, Y. Chen, E.A. Marquis, E. Bordas, P. Trocellier, Y. Serruys, A. Gentils, O.
778 Kaïtasov, Y. De Carlan, A. Legris, Radiation-induced Ostwald ripening in oxide dispersion
779 strengthened ferritic steels irradiated at high ion dose, *Acta Mater.* 78 (2014) 328–340.
780 doi:10.1016/j.actamat.2014.06.060.
- 781 [49] M.L. Lescoat, J. Ribis, Y. Chen, E.A. Marquis, E. Bordas, P. Trocellier, Y. Serruys, A. Gentils, O.
782 Kaïtasov, Y. De Carlan, A. Legris, Radiation-induced Ostwald ripening in oxide dispersion
783 strengthened ferritic steels irradiated at high ion dose, *Acta Mater.* 78 (2014) 328–340.
784 doi:10.1016/j.actamat.2014.06.060.
- 785 [50] Z. Zheng, T.A. Saleh, S.A. Maloy, O. Anderoglu, Microstructure evolution in MA956 neutron
786 irradiated in ATR at 328 °C to 4.36 dpa, *J. Nucl. Mater.* 533 (2020).
- 787 [51] T. Chen, H. Kim, J.G. Gigax, D. Chen, C.C. Wei, F.A. Garner, L. Shao, Radiation response of
788 oxide-dispersion-strengthened alloy MA956 after self-ion irradiation, *Nucl. Instruments Methods*
789 *Phys. Res. Sect. B Beam Interact. with Mater. Atoms.* 409 (2017) 259–263.
790 doi:10.1016/j.nimb.2017.05.024.
- 791 [52] T. Chen, E. Aydogan, J.G. Gigax, D. Chen, J. Wang, X. Wang, S. Ukai, F.A. Garner, L. Shao,
792 Microstructural changes and void swelling of a 12Cr ODS ferritic-martensitic alloy after high-dpa
793 self-ion irradiation, *J. Nucl. Mater.* 467 (2015) 42–49. doi:10.1016/j.jnucmat.2015.09.016.
- 794 [53] E. Aydogan, N. Almirall, G.R. Odette, S.A. Maloy, O. Anderoglu, L. Shao, J.G. Gigax, L. Price,
795 D. Chen, T. Chen, F.A. Garner, Y. Wu, P. Wells, J.J. Lewandowski, D.T. Hoelzer, Stability of
796 nanosized oxides in ferrite under extremely high dose self ion irradiations, *J. Nucl. Mater.* 486
797 (2017) 86–95. doi:10.1016/j.jnucmat.2017.01.015.
- 798 [54] E. Getto, K. Sun, A.M. Monterrosa, Z. Jiao, M.J. Hackett, G.S. Was, Void swelling and
799 microstructure evolution at very high damage level in self-ion irradiated ferritic-martensitic steels,
800 *J. Nucl. Mater.* 480 (2016) 159–176. doi:10.1016/j.jnucmat.2016.08.015.
- 801 [55] T. Chen, E. Aydogan, J.G. Gigax, D. Chen, J. Wang, X. Wang, S. Ukai, F.A. Garner, L. Shao,
802 Microstructural changes and void swelling of a 12Cr ODS ferritic-martensitic alloy after high-dpa
803 self-ion irradiation, *J. Nucl. Mater.* 467 (2015) 42–49. doi:10.1016/j.jnucmat.2015.09.016.
- 804 [56] M.B. Toloczko, F.A. Garner, V.N. Vovyevodin, V.V. Bryk, O.V. Borodin, V.V. Mel'nychenko,
805 A.S. Kalchenko, Ion-induced swelling of ODS ferritic alloy MA957 tubing to 500 dpa, *J. Nucl.*
806 *Mater.* 453 (2014) 323–333. doi:10.1016/j.jnucmat.2014.06.011.
- 807 [57] F.A. Smidt, P.R. Malmberg, J.A. Sprague, J.E. Westmoreland, Swelling Behavior of Commercial
808 Ferritic Alloys, Em-12 and Ht-9, As Assessed By Heavy Ion Bombardment., *ASTM Spec. Tech.*
809 *Publ.* (1976) 227–241.
- 810 [58] J.J. Kai, G.L. Kulcinski, 14 MeV nickel-ion irradiated HT-9 ferritic steel with and without helium
811 pre-implantation, *J. Nucl. Mater.* 175 (1990) 227–236. doi:10.1016/0022-3115(90)90211-5.
- 812 [59] C.H. Zhang, Y.T. Yang, Y. Song, J. Chen, L.Q. Zhang, J. Jang, A. Kimura, Irradiation response of
813 ODS ferritic steels to high-energy Ne ions at HIRFL, *J. Nucl. Mater.* 455 (2014) 61–67.
814 doi:10.1016/j.jnucmat.2014.04.015.
- 815 [60] F.A. Garner, Radiation-Induced Damage in Austenitic Structural Steels Used in Nuclear Reactors,
816 2020. doi:10.1016/b978-0-12-803581-8.12067-3.
- 817 [61] M. West, B. Jasthi, P. Hosemann, V. Sodesetti, Friction Stir Welding of Oxide Dispersion
818 Strengthened Alloy MA956, in: *Frict. Stir Weld. Process. VI*, 2011: pp. 33–40.
- 819 [62] C.L. Chen, G.J. Tatlock, A.R. Jones, Microstructural evolution in friction stir welding of
820 nanostructured ODS alloys, *J. Alloys Compd.* 504 (2010) S460–S466.
821 doi:10.1016/j.jallcom.2010.02.192.
- 822 [63] W. Han, P. Liu, X. Yi, Q. Zhan, F. Wan, K. Yabuuchi, H. Serizawa, A. Kimura, Impact of friction
823 stir welding on recrystallization of oxide dispersion strengthened ferritic steel, *J. Mater. Sci.*
824 *Technol.* (2017). doi:10.1016/j.jmst.2017.11.032.
- 825 [64] D.S. Gelles, Microstructural examination of commercial ferritic alloys at 200 dpa, *J. Nucl. Mater.*
826 233–237 (1996) 293–298. doi:10.1016/S0022-3115(96)00222-X.

- 827 [65] A.M. Dvoriashin, S.I. Porollo, Y. V. Konobeev, F.A. Garner, Influence of high dose neutron
828 irradiation on microstructure of EP-450 ferritic-martensitic steel irradiated in three Russian fast
829 reactors, *J. Nucl. Mater.* 329–333 (2004) 319–323. doi:10.1016/j.jnucmat.2004.04.309.
- 830 [66] M. Song, Y.D. Wu, D. Chen, X.M. Wang, C. Sun, K.Y. Yu, Y. Chen, L. Shao, Y. Yang, K.T.
831 Hartwig, X. Zhang, Response of equal channel angular extrusion processed ultrafine-grained T91
832 steel subjected to high temperature heavy ion irradiation, *Acta Mater.* 74 (2014) 285–295.
833 doi:10.1016/j.actamat.2014.04.034.
- 834 [67] D.T. Hoelzer, C.P. Massey, S.J. Zinkle, D.C. Crawford, K.A. Terrani, Modern nanostructured
835 ferritic alloys: A compelling and viable choice for sodium fast reactor fuel cladding applications,
836 *J. Nucl. Mater.* 529 (2020) 1–12.
- 837 [68] S.J. Zinkle, J.L. Boutard, D.T. Hoelzer, A. Kimura, R. Lindau, G.R. Odette, M. Rieth, L. Tan, H.
838 Tanigawa, Development of next generation tempered and ODS reduced activation
839 ferritic/martensitic steels for fusion energy applications, *Nucl. Fusion.* 57 (2017) 92005.
840 doi:10.1088/1741-4326/57/9/092005.
- 841 [69] R.L. Klueh, D.R. Harries, High-Chromium Ferritic and Martensitic Steels for Nuclear
842 Applications, 2001. doi:10.1520/MONO3-EB.
- 843 [70] E. Getto, Z. Jiao, A.M. Monterrosa, K. Sun, G.S. Was, Effect of irradiation mode on the
844 microstructure of self-ion irradiated ferritic-martensitic alloys, *J. Nucl. Mater.* 465 (2015) 116–
845 126. doi:10.1016/j.jnucmat.2015.05.016.
- 846 [71] E. Getto, Z. Jiao, A.M. Monterrosa, K. Sun, G.S. Was, Effect of pre-implanted helium on void
847 swelling evolution in self-ion irradiated HT9, *J. Nucl. Mater.* 462 (2015) 458–469.
848 doi:10.1016/j.jnucmat.2015.01.045.
- 849 [72] A.M. Monterrosa, Z. Jiao, G.S. Was, The influence of helium on cavity evolution in ion-irradiated
850 T91, *J. Nucl. Mater.* 509 (2018) 707–721. doi:10.1016/j.jnucmat.2018.06.033.
- 851 [73] Z. Jiao, S. Taller, K.G. Field, G. Yeli, M.P. Moody, G.S. Was, Microstructure evolution of T91
852 irradiated in the BOR60 fast reactor, *J. Nucl. Mater.* 504 (2018) 122–134.
- 853 [74] A.A. Kohnert, H. Tummala, R.A. Lebensohn, C.N. Tome, L. Capolungo, On the use of
854 transmission electron microscopy to quantify dislocation densities in bulk metals, (2021).
- 855 [75] E.M. Getto, The Co-Evolution of Microstructure Features in Self-Ion Irradiated HT9 at Very High
856 Damage Levels (Doctoral Thesis, University of Michigan, Ann Arbor, MI), University of
857 Michigan, 2016. doi:2027.42/135912.
- 858 [76] N. Anento, A. Serra, Carbon-vacancy complexes as traps for self-interstitial clusters in Fe-C
859 alloys, *J. Nucl. Mater.* 440 (2013) 236–242. doi:10.1016/j.jnucmat.2013.04.087.
- 860 [77] S. Taller, G.S. Was, Understanding bubble and void nucleation in dual ion irradiated T91 steel
861 using single parameter experiments, *Acta Mater.* 198 (2020) 47–60.
862 doi:10.1016/j.actamat.2020.07.060.
- 863